

# Evaluation of local similarity theory in the wintertime nocturnal boundary layer over heterogeneous surface

---

**Babić, Karmen; Rotach, Mathias W.; Bencetić Klaić, Zvezdana**

*Source / Izvornik:* **Agricultural and Forest Meteorology, 2016, 228-229, 164 - 179**

**Journal article, Accepted version**

**Rad u časopisu, Završna verzija rukopisa prihvaćena za objavljivanje (postprint)**

<https://doi.org/10.1016/j.agrformet.2016.07.002>

*Permanent link / Trajna poveznica:* <https://um.nsk.hr/um:nbn:hr:217:291336>

*Rights / Prava:* [In copyright](#) / [Zaštićeno autorskim pravom.](#)

*Download date / Datum preuzimanja:* **2025-03-31**



*Repository / Repozitorij:*

[Repository of the Faculty of Science - University of Zagreb](#)



# Evaluation of Local Similarity Theory in the Wintertime Nocturnal Boundary Layer over Heterogeneous Surface

Karmen Babić<sup>1</sup>, Mathias W. Rotach<sup>2</sup> and Zvezdana B. Klaić<sup>1</sup>

<sup>1</sup> *Department of Geophysics, Faculty of Science, University of Zagreb, Zagreb, Croatia.*

<sup>2</sup> *Institute of Atmospheric and Cryospheric Sciences, University of Innsbruck, Innsbruck, Austria.*

**Abstract:** The local scaling approach was examined based on the multi-level measurements of atmospheric turbulence in the wintertime (December 2008– February 2009) stable atmospheric boundary layer (SBL) established over a heterogeneous surface influenced by mixed agricultural, industrial and forest surfaces. The heterogeneity of the surface was characterized by spatial variability of both roughness and topography. Nieuwstadt's local scaling approach was found to be suitable for the representation of all three wind velocity components. For neutral conditions, values of all three non-dimensional velocity variances were found to be smaller at the lowest measurement level and larger at higher levels in comparison to classical values found over flat terrain. Influence of surface heterogeneity was reflected in the ratio of observed dimensionless standard deviation of the vertical wind component and corresponding values of commonly used similarity formulas for flat and homogeneous terrain showing considerable variation with wind direction. The roughness sublayer influenced wind variances, and consequently the turbulent kinetic energy and correlation coefficients at the lowest measurement level, but not the wind shear profile. The observations support the classical linear expressions for the dimensionless wind shear ( $\phi_m$ ) even over inhomogeneous terrain after removing data points associated with the flux Richardson number ( $Rf$ ) greater than 0.25. Leveling-off of  $\phi_m$  at higher stabilities was found to be a result of the large number of data characterized by small-scale turbulence ( $Rf > 0.25$ ). Deviations from linear expressions were shown to be mainly due to this small-scale turbulence rather than due to the surface heterogeneities, supporting the universality of this relationship. Additionally, the flux-gradient dependence on stability did not show different behavior for different wind regimes, indicating that the stability parameter is sufficient predictor for flux-gradient relationship. Data followed local  $z$ -less scaling for  $\phi_m$  when the prerequisite  $Rf \leq 0.25$  was imposed.

Key words: Stable boundary layer, Local scaling, Forest canopy, Roughness sublayer, Turbulent kinetic energy

Corresponding author at: Department of Geophysics, Faculty of Science, University of Zagreb,

Horvatovac 95, 10000 Zagreb, Croatia. Tel: +385 1 460 59 26.

E-mail address: babick@gfz.hr (K. Babić)

©2016. This manuscript version is made available under the CC-BY-NC-ND 4.0 licence

<http://creativecommons.org/licenses/by-nc-nd/4.0/>

## 32 **1. Introduction**

33 Stable atmospheric boundary layers (SBLs) are influenced by many independent forcings, such as,  
34 (sub)mesoscale motions, which act on a variety of time and space scales, net radiative cooling, temperature  
35 advection, surface roughness and surface heterogeneity (Mahrt, 2014) enhancing the complexities and  
36 posing challenges in the study of the SBL. The fate of pollutants in the boundary layer is strongly affected  
37 by turbulence which is extremely complicated in complex terrain and over heterogeneous surfaces.  
38 Moreover, due to weak turbulence the SBL is generally favorable for the establishment of air pollution  
39 episodes. Atmospheric dispersion models, used for air quality studies, as well as high-resolution regional  
40 models use similarity scaling to model flow characteristics and dispersion in such environments.

41 Monin-Obukhov similarity theory (MOST) (Monin and Obukhov, 1954; Obukhov, 1946) relates surface  
42 turbulent fluxes to vertical gradients, variances and scaling parameters. The assumptions underlying MOST  
43 include stationary atmospheric turbulence, surface homogeneity and the existence of an inertial sublayer  
44 (that is, surface layer, SL). Relations between these parameters (Businger et al., 1971; Dyer, 1974) are based  
45 on several experimental campaigns conducted over horizontally homogeneous and flat (HHF) surfaces  
46 (Kaimal and Wyngaard, 1990), where the original assumptions are considered to be met. Originally, MOST  
47 was based on surface fluxes, which were assumed to be constant with height, and equal to surface values  
48 within the SL (also referred to as constant-flux layer). In the unstable boundary layer, MOST has been  
49 extensively studied and proven useful in relating turbulent fluxes to profiles (Businger et al., 1971; Dyer,  
50 1974; Wyngaard and Coté, 1972). However, the applicability of MOST in the stable SL (e.g. Cheng et al.,  
51 2005; Trini Castelli and Falabino, 2013) and over complex (Babić et al., 2016; Nadeau et al., 2013; Stiperski  
52 and Rotach, 2016) and heterogeneous surfaces is still an open issue due to many difficulties when applying  
53 traditional scaling rules since MOST assumptions may not be fulfilled. Nieuwstadt (1984) extended Monin-  
54 Obukhov similarity in terms of a local scaling approach. This regime represents the extension of MOST  
55 above the SL. Accordingly, all MOST variables are based on the local fluxes at a certain height  $z$  instead of  
56 using surface values. As MOST should be valid over flat and homogeneous terrain, studies of the SBL in  
57 terms of surface layer and local scaling approaches were made over areas characterized by long and uniform  
58 fetch conditions, such as, Greenland, Arctic pack ice and Antarctica (Forrer and Rotach, 1997; Grachev et  
59 al., 2013, 2007; Sanz Rodrigo and Anderson, 2013). Forrer and Rotach (1997) concluded that local scaling is  
60 superior over surface layer scaling. This was mainly due to the fact that surface layer over an ice sheet, with

61 continuously stable stratification, can be very shallow ( $< 10$  m). Moreover, for cases of strong stability, non-  
62 dimensional similarity functions for momentum and heat were in agreement with the results obtained from  
63 the local scaling approach. Grachev et al. (2013) examined limits of applicability of local similarity theory in  
64 the SBL by revisiting the concept of a critical Richardson number.

65 Even modest surface heterogeneity can significantly influence the nocturnal boundary layer (NBL) and  
66 lead to turbulence at higher Richardson numbers in comparison with homogeneous surfaces (Derbyshire,  
67 1995). Since the earth's solid surfaces are mainly heterogeneous (at least to a certain degree), the interest in  
68 flow and turbulence characteristics over complex surfaces has increased in recent decades. Moreover, a  
69 proper representation of turbulence is particularly important for parameterization of surface-atmosphere  
70 exchange processes in atmospheric models (e.g., dispersion, numerical weather prediction or regional  
71 models). The turbulence characteristics have been studied through direct measurements for different  
72 complex surfaces including, complex forest sites (e.g. Dellwik and Jensen, 2005; Nakamura and Mahrt,  
73 2001; Rannik, 1998), agricultural fields, such as, apple orchard (e.g. de Franceschi et al., 2009) or rice  
74 plantation (e.g. Moraes et al., 2005), metre-scale inhomogeneity (Andreas et al., 1998a), urban areas (e.g.  
75 Fortuniak et al., 2013; Wood et al., 2010), and complex mountainous terrains (e.g. Rotach et al., 2008),  
76 addressing to both valley floors (e.g. de Franceschi et al., 2009; Moraes et al., 2005; Rotach et al., 2004) and  
77 steep slopes (Nadeau et al., 2013; Stiperski and Rotach, 2016). However, most of these studies are  
78 associated with flows over homogeneous surfaces. In recent years much effort has been put into simulations  
79 of turbulent fluxes over relatively heterogeneous surfaces using large-eddy simulations (LES, e.g. Calaf et  
80 al., 2014). Bou-Zeid et al. (2007) used LES over surfaces with varying roughness lengths to assess the  
81 parameterization for the equivalent surface roughness and the blending height in the neutral boundary layer  
82 at regional scales. Large eddy simulations of surface heterogeneity effects on regional scale fluxes and  
83 turbulent mixing in the stably stratified boundary layers were studied by Miller and Stoll, 2013; Mironov  
84 and Sullivan, 2010; Stoll and Porté-Agel, 2008.

85 The vertical structure of the atmospheric boundary layer is traditionally partitioned into a SL, an outer  
86 layer and the entrainment zone (e.g. Mahrt, 2000). The SL, in turn, is subdivided into a canopy layer (CL), a  
87 roughness sublayer (RSL) and inertial sublayer. Over surfaces with small roughness elements the latter,  
88 which corresponds to the true equilibrium layer, is often identified with SL. These concepts are less  
89 applicable over heterogeneous surfaces but for the SBL they provide, nevertheless, a useful starting point.

90 Above very rough surfaces, such as forests or agricultural crops, the RSL has a non-negligible extension.  
91 Due to the influence of individual roughness elements on the flow within the RSL (e.g. Finnigan, 2000;  
92 Katul et al., 1999), MOST is not widely accepted. The existence of large-scale coherent turbulent structures  
93 within the RSL, which are generated at the canopy top through an inviscid instability mechanism (Raupach  
94 et al., 1996), is thought to be a reason for the failure of standard flux-gradient relationships (Harman and  
95 Finnigan, 2010).

96 In the scientific community substantial effort was made to address MOST in different conditions. Most  
97 of the observational studies are based on measurements from a single tower, and sometimes they result in  
98 inconsistent conclusions on the applicability of similarity theory. These inconsistencies are mostly found for  
99 studies of MOST in complex terrain (e.g. de Franceschi et al., 2009; Kral et al., 2014; Martins et al., 2009;  
100 Nadeau et al., 2013) or for small scale turbulence for which  $z$ -less scaling regime should apply (e.g. Basu et  
101 al., 2006; Cheng and Brutsaert, 2005; Forrer and Rotach, 1997; Grachev et al., 2013; Pahlow et al., 2001).  
102 The main objective of the present paper is to examine the applicability of local similarity scaling over a  
103 heterogeneous terrain influenced by a mixture of forest, agricultural and industrial surfaces, based on multi-  
104 level turbulence observations in the wintertime SBL. Many of the above mentioned studies in complex  
105 terrain are mainly characterized by homogeneous surface roughness, while studies over heterogeneous and  
106 patchy vegetation are still scarce in the literature. Additionally, this paper relates to the approach of Grachev  
107 et al. (2013), who investigated the limits of applicability of local similarity theory in the SBL over idealized  
108 homogeneous surface of the Arctic pack ice. In the present work we use their approach to distinguish  
109 between Kolmogorov and non-Kolmogorov turbulence, and consequently, to investigate whether classical  
110 linear flux-gradient relationships can be applied for non-homogeneous surfaces. The paper is organized as  
111 follows: in Section 2, we give a brief overview of the local scaling approach. In Section 3, we describe the  
112 measurement site and measurements and we provide a description of post processing procedures. Section 4  
113 contains our results for scaled standard deviations of wind components, turbulent kinetic energy, turbulent  
114 exchange coefficients and non-dimensional wind profile. A summary and conclusions are given in Section 5.

115

## 116 **2. Local scaling**

117 Holtslag and Nieuwstadt (1986) presented an overview of scaling regimes for the SBL. Each of the  
118 scaling regimes is characterized by different scaling parameters. The turbulence in the SL can be described

119 by MOST with surface fluxes of heat and momentum and the height  $z$  as scaling parameters. In this layer  
 120 the relevant scaling parameter is the Obukhov length  $L$  (Obukhov, 1946), given by

$$L = -\frac{u_*^3}{k \frac{g}{\theta_v} (\overline{w'\theta'_v})_s} \quad (1)$$

121 where  $u_* = (\overline{u'w'_s}^2 + \overline{v'w'_s}^2)^{1/4}$  is the surface friction velocity,  $(\overline{w'\theta'_v})_s$  is the surface kinematic heat  
 122 flux,  $\overline{\theta_v}$  is the virtual potential temperature,  $g$  is the acceleration due to the gravity,  $k=0.4$  is the von Kármán  
 123 constant. Overbars and primes denote time averaging and fluctuating quantities, respectively.

124 Above the SL, the local scaling regime applies, a regime proposed by Nieuwstadt (1984). According to  
 125 Nieuwstadt's local similarity approach, properly scaled turbulence statistics should solely be a function of the  
 126 local stability parameter  $\zeta_l = (z - d)/\Lambda$ , where  $z$  is the measurement height,  $d$  is zero-plane displacement  
 127 height and  $\Lambda$  is the local Obukhov length. Even if Nieuwstadt (1984) was not referring to rough surfaces, we  
 128 have introduced  $d$  as we will be concerned with data from a site where the canopy height is non-negligible.  
 129 In the local scaling framework, the local Obukhov length is based on the local fluxes at height  $z$  and varies  
 130 with height

$$\Lambda = -\frac{u_{*l}^3}{k \frac{g}{\theta_v} \overline{w'\theta'_v}} \quad (2)$$

131 where  $u_{*l}$  indicates local friction velocity and  $\overline{w'\theta'_v}$  is the local heat flux. Holtslag and Nieuwstadt (1986,  
 132 their Fig. 2) showed that in the part of the SBL which encompasses a layer between 10 and 50 % of the total  
 133 BL height at neutral stability and is exponentially decreasing with increasing stability,  $\Lambda \approx L$ . This indicates  
 134 that the use of  $(z-d)/\Lambda$ , which is required by local scaling, is almost equivalent to the SL scaling parameter  $(z-$   
 135  $d)/L$ . Therefore, the local scaling approach can be viewed as an extension of MOST for the entire SBL.

136 For large values of  $z/\Lambda$  ( $z/\Lambda \rightarrow \infty$ ), the dependence on  $z$  disappears because stable stratification restricts  
 137 vertical motion causing turbulence scales to be very small. Wyngaard and Coté (1972) named this limit  
 138 "local z-less stratification" (height-independent). Based on the observations from a tall tower (Cabauw),  
 139 Nieuwstadt (1984) found this limit to be for  $\zeta_l > 1$ .

140 Evaluation of second-order moments, especially of wind velocity standard deviations provides a good  
 141 understanding of turbulence statistics. According to similarity theory, dimensionless quantities should be  
 142 universal functions of the non-dimensional stability parameter. In the local scaling framework, standard

143 deviations of wind speed components  $\sigma_i$ , where  $i = (u, v, w)$  denotes longitudinal, lateral and vertical  
 144 velocity components, respectively, are scaled as

$$\phi_i = \frac{\sigma_i}{u_{*l}} \quad (3)$$

145 where  $\phi_i$  represents a set of universal similarity functions, different for each velocity component. In the  
 146 literature different formulations of the  $\phi_i$  functions can be found. de Franceschi et al. (2009) presented a  
 147 comprehensive review of various formulations of  $\phi_i$  functions suggested by different studies and for  
 148 different stabilities. A generally accepted form of the flux-variance similarity relationships in the stable  
 149 boundary layer is

$$\phi_i(\zeta_l) = a_i(1 + b_i\zeta_l)^{c_i} \quad (4)$$

150 where coefficients  $a_i$ ,  $b_i$  and  $c_i$  need to be found experimentally. Accordingly, the non-dimensional wind  
 151 shear defined as

$$\phi_m(\zeta_l) = \frac{k(z-d)}{u_{*l}} \frac{\partial U}{\partial z} \quad (5)$$

152 where  $U$  is the mean wind speed, is also a unique function of stability. For neutral conditions ( $\zeta = 0$ ),  $\phi_m$   
 153 approaches unity. As the exact forms of the similarity functions are not predicted by similarity theory and  
 154 they should be determined from field experiments, many different formulations have been proposed based  
 155 on the data from different experiments (e.g. Beljaars and Holtslag, 1991; Cheng and Brutsaert, 2005; Dyer,  
 156 1974; Grachev et al., 2007; Sorbjan and Grachev, 2010). We will compare our results to the linear  
 157 relationship of Dyer (1974) obtained for the stable SL

$$\phi_m(z/L) = 1 + b_m \frac{z}{L} \quad (6)$$

158 where  $b_m = 5$ . Högström (1988) modified several existing formulas for  $\phi_m$  (and also for the non-  
 159 dimensional temperature profile,  $\phi_h$ ), in order to comply with his assumptions of  $k = 0.4$  and  $(\phi_h)_{\zeta=0} =$   
 160  $0.95$ . For Dyer's expression (6), he obtained a value  $b_m = 4.8$ . Additionally, we compare our results to the  
 161 non-linear stability function of Beljaars and Holtslag (1991)

$$\phi_m(z/L) = 1 + a \frac{z}{L} + b \frac{z}{L} e^{-d \frac{z}{L}} - bd \frac{z}{L} \left( \frac{z}{L} - \frac{c}{d} \right) e^{-d \frac{z}{L}} \quad (7)$$

162 where  $a = 1$ ,  $b = 0.667$ ,  $c = 5$ ,  $d = 0.35$ , as expressions (6) and (7) are probably the most often used for  
 163 parameterization in numerical models. Both relationships were derived over flat and homogeneous terrain  
 164 using Obukhov length, which is based on surface values. While the first expression was derived and verified

165 by different experiments in the stability range  $0 < z/L < 1$ , Eq. (7) is valid in strongly stable conditions were  
 166 the overestimation of the non-dimensional gradients is reduced. Linear equations for the stable SL together  
 167 with the relations for the unstable conditions are traditionally called Businger-Dyer relations (Businger et al.,  
 168 1971; Dyer, 1974). Similar to the non-dimensional velocity variances we use the non-dimensional wind  
 169 shear in its local form (see Eq. (5)).

170 Another widely used stability parameter is the flux Richardson number, defined based on the vertical  
 171 gradient of wind speed

$$Rf = \frac{-\frac{g}{\theta_v} \overline{w'\theta'_v}}{u_*^2 \frac{\partial U}{\partial z}}. \quad (8)$$

172 Grachev et al. (2013) argued that the upper limit for applicability of the local similarity theory is determined  
 173 by the inequalities  $Ri < Ri_{cr}$  and  $Rf < Rf_{cr}$ , where  $Ri$  is the gradient Richardson number. They found both  
 174 critical values to be equal to  $Ri_{cr} = Rf_{cr} = 0.20 - 0.25$ , with  $Rf_{cr} = 0.20 - 0.25$  being the primary  
 175 threshold. The  $z$ -less concept requires that  $z$  cancels in Eqs. (4) and (6). As a result, a linear relationship for  
 176 the non-dimensional function  $\phi_m$  is obtained, while non-dimensional functions  $\phi_i$  asymptotically approach  
 177 constant values:

$$\phi_m(\zeta_l) = b_m \zeta_l, \quad (9)$$

$$\phi_i = b_i, \quad (10)$$

178 where  $b_m$  and  $b_i$  are experimentally determined coefficients. For convenience, throughout this paper we will  
 179 use the notation  $\zeta = \zeta_l$  as all variables are based on local values.

180

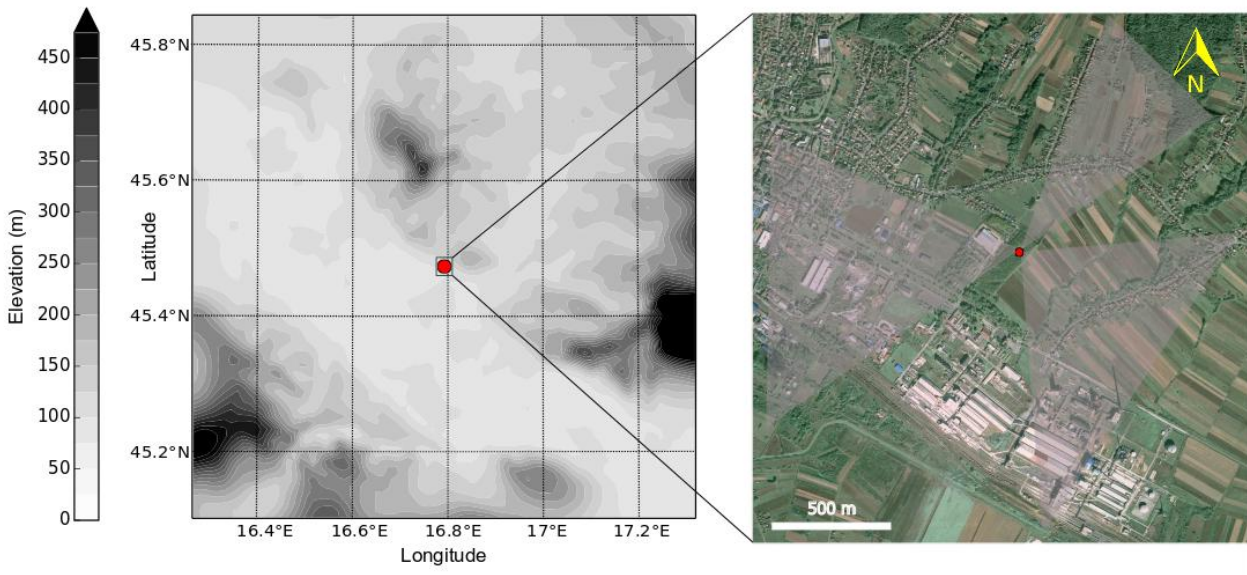
### 181 3. Data and Methods

#### 182 3.1. Site description

183 A 62 m high tower was located in the vicinity of the small industrial town Kutina, Croatia (tower  
 184 coordinates: 45°28'32"N, 16°47'44"E). The tower was placed above a grassy surface and it was surrounded  
 185 by approximately 18 m high black walnut (*Juglans nigra*) trees. The closest trees are approximately 20–25  
 186 m away from the tower and they encompass an area of approximately 120–480 m<sup>2</sup> (Fig. 1). The tower is  
 187 situated in a rather heterogeneous surrounding regarding both a larger spatial scale (Fig. 1a) and immediate  
 188 vicinity of the measurement site (on the order of 1 km distance, Fig. 1b). To the east of the tower, crop



189 fields, which extend to the aerial distance of more than 1 km, are found. South-southeast of the tower, about  
 190 800 m to 1.5 km distant a large petrochemical industry plant is placed. In a sector that encounters winds  
 191 from the north-northwest to the northeast, low, forested hills are located. They are covered with a dense  
 192 forest, while at lower elevations, cultivated orchards and vineyards are found. Fooths of these hills are  
 193 roughly 1.3 km away from the measurement site. Thus, due to different surface roughness features  
 194 measurements in the SBL at the measuring site may be contaminated by local advective fluxes, drainage  
 195 flows and/or orographically-generated gravity waves. These features are related to (sub)mesoscale motions  
 196 which do not obey similarity scaling and are therefore removed from our data by the rigorous data quality  
 197 control and post-processing options as described later in the paper (Section 3.2.). We are thus focusing on  
 198 the micrometeorologically complex local site characteristics, which may be more typical for real sites than  
 199 the usually investigated homogeneous reference sites.



200  
 201 **Fig. 1.** (a) Topographic map with contour lines each 25 m of the area surrounding the measurement site (red  
 202 dot) representing inhomogeneous terrain on a larger spatial scale. (b) Google Maps image (Image © 2015  
 203 DigitalGlobe) of the observational site. Measurement tower is indicated with a red dot (45°28'32"N,  
 204 16°47'44"E). Light gray shaded areas correspond to wind directions depicted in Fig. 5.  
 205

206 Data used in this study were collected during wintertime (1 December 2008–28 February 2009) and  
 207 correspond to the nocturnal period from 1800 to 0600 local time. Turbulence measurements of three-  
 208 dimensional wind and sonic temperature were continuously measured using identical WindMaster Pro (Gill  
 209 Instruments) ultrasonic anemometers that sampled at 20 Hz. Data were measured at five levels above the

210 canopy height, hereafter at level 1 ( $z_1 = 20$  m above the surface), level 2 ( $z_2 = 32$  m), level 3 ( $z_3 = 40$  m),  
 211 level 4 ( $z_4 = 55$  m) and level 5 ( $z_5 = 62$  m). Measurement levels were prescribed prior to the experiment  
 212 through existing tower infrastructure. Given the complicated and spatially inhomogeneous characteristics of  
 213 the measurement site, an idealized vertical structure is considered as a zero-order approach in the analysis.  
 214 Estimate of vertical layers for neutral conditions was done using different models available in the literature  
 215 and serves as a simple model for the interpretation of the results. For stably stratified conditions these  
 216 estimates will not be perfectly appropriate, but will provide the gross picture.

217 Conceptually, when the air flows over changing terrain, the downwind surface conditions are likely to  
 218 influence the measurements via internal boundary layers (IBLs), which grow in height ( $h_i$ ) with downwind  
 219 distance (Fig. 2) (e.g. Cheng and Castro, 2002; Dellwik and Jensen, 2005). Only the lowest portion of the  
 220 IBL (10%) is in equilibrium with the new surface (internal equilibrium layer, IEL) while the flow above the  
 221 IBL is in equilibrium with the upstream surface conditions. The IEL can, finally, be identified with the  
 222 inertial sublayer (IS). However, if the new surface is very rough its lower part must be considered as a RSL.  
 223 Within the upper part of the IEL, i.e. IS, turbulent fluxes are approximately constant with height, MOST is  
 224 valid and the mean wind speed follows the expected logarithmic profile. Within the RSL, the flow is  
 225 influenced by the distribution and structure of canopy elements (Monteith and Unsworth, 1990; Rotach and  
 226 Calanca, 2014), with momentum and scalars transported by turbulence, wake effects and molecular diffusion  
 227 (Malhi, 1996). Above the height of the IEL ( $h_e$ ) stress and fluxes start to decrease due to the upwind  
 228 influence. This layer is defined as a transition layer (Fig. 2). Due to the very tall roughness elements we use  
 229 the zero-plane displacement height ( $d$ ) as our reference - hence the IBL is assumed to range from  $z = d$  up  
 230 to  $z = h_i + d$ . Ideally, after a long enough flow over the new surface the IBL fills the entire boundary layer.  
 231 Since we are interested in evaluating the degree to which local scaling applies under inhomogeneous fetch  
 232 conditions we map the idealized SBL structure to the IBL. The transition layer then becomes the outer part  
 233 of the inhomogeneously forced SBL.

234 We have estimated the length scales introduced above as follows:  $h_i$  is estimated based on the model of  
 235 Cheng and Castro (2002)

$$\frac{h_i}{z_{02}} = 10.56 \left( \frac{x}{z_{02}} \right)^{0.33}, \quad (11)$$

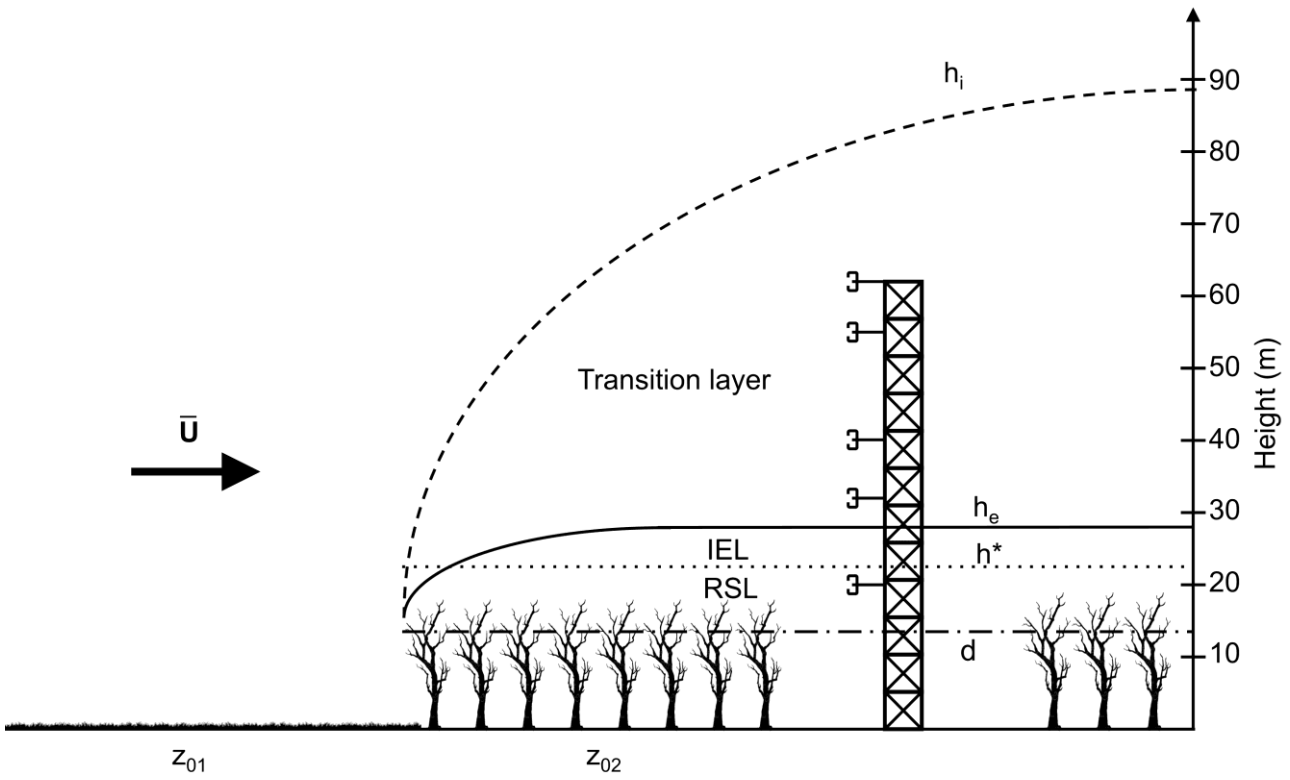


**Fig. 2.** Conceptual sketch of idealized vertical layers after a step change in surface roughness for the long fetch case (391 m) under neutral conditions. The height of the IBL ( $h_i$ ), which develops due to the change in roughness conditions, is estimated based on the model of Cheng and Castro (2002). Above the  $h_i$  the flow is in equilibrium with the upwind surface. Within the internal equilibrium layer (IEL) the flow is in equilibrium with the forest. The transition layer indicates the transition zone between upwind and downwind equilibrium conditions. The dotted line denotes the height of the RSL,  $h^*$ , estimated based on relation of Raupach (1994). The dash-dot line shows the zero-plane displacement height ( $d$ ) estimated as  $3/4h_c$  (Kaimal and Finnigan, 1994; Stull, 1988).  $z_{01}$  and  $z_{02}$  correspond to upwind and downwind roughness lengths, respectively. The black arrow denotes the mean wind ( $U$ ) direction.

where  $x$  is the distance to the roughness change from the position of measurement (fetch) and  $z_{02}$  is the roughness length of the new surface. Following Cheng and Castro (2002),  $h_e$  can be determined as

$$\frac{h_e}{z_{02}} = 1.47 \left( \frac{x}{z_{02}} \right)^{0.37}. \quad (12)$$

The depth of the RSL ( $h^*$ ) depends on different properties, such as canopy density, roughness length for momentum and tree height. Raupach (1994) estimated the height of the RSL as

$$\frac{h^* - d}{h_c - d} = 2. \quad (13)$$

For the zero-plane displacement we use a straightforward methodology,  $d = \frac{3}{4}h_c$  (Kaimal and Finnigan, 1994; Stull, 1988), where  $h_c = 18$  m is the average canopy height, which is estimated through direct

253 measurements (using laser distance meter). Additionally, for the walnut forest we used  $z_{02} = 1$  m (the lower  
 254 value for the roughness length over forest,  $z_0 = 1$  m, according to Foken (2008), his Table 3.1).

255 The estimated height of the IBL at our site (Tab. 1) varied between 40 and 76 m for short ( $\approx 56$  m) and  
 256 long ( $\approx 390$  m) fetch conditions, respectively. Estimated values of  $h_e$  at the location of the tower ranged  
 257 between 6.5 and 13.7 m according to Cheng and Castro (2002) for short and long fetch cases, respectively.

258

259 **Table 1**

260 Height of the equilibrium layer ( $h_e$ ) and of the internal boundary layer ( $h_i$ ) estimated based on the model of  
 261 the Cheng and Castro (2002) (Eqs. (11) and (12)) for different fetch ( $x$ ) values corresponding to particular  
 262 wind directions (WD). Note that these heights indicate the height above the displacement height  $d$ . In the  
 263 determination of the fetch length, holes in the forest or corridors of vegetation other than forest were  
 264 disregarded if their size was small enough.

WD (deg)	30	60	90	120	150	180	210	240	270	300	330	360
$x$ (m)	92	89	69	56	58	77	391	415	110	84	78	105
$h_e$ (m)	7.8	7.7	7.0	6.5	6.6	7.3	13.4	13.7	8.3	7.6	7.4	8.2
$h_i$ (m)	47	46	43	40	40	44	76	77	50	46	44	49

265

266 These estimates indicate that the second measurement level is above the IEL height ( $z = h_i + d$ ) for all  
 267 wind directions. Also, the height of the RSL at our measurement site is  $h^* = 1.25h_c$ , that is, approximately  
 268 22.5 m. Using the above estimates, we find that level 1 is likely to be within the RSL for all wind directions.  
 269 For cases characterized with the short fetch, the IEL will most likely be within the RSL ( $h_e + d < h^*$ ),  
 270 while only for wind direction with large fetch conditions (200–250 deg) the growing equilibrium layer will  
 271 encompass the RSL and a thin IS will form. Levels 2 and 3 are in the transition layer for all wind directions,  
 272 while levels 4 and 5 are even above  $h_i$  for the short fetches (105–175 deg). The highest measurement level  
 273 reflects the upwind surface conditions for fetches shorter than 100 m. Hence a potential RSL influence  
 274 should be detectable if level 1 behaves differently. If levels 2–5 do not show different behavior this can be  
 275 taken as an indication that our crude mapping assumption has some validity.

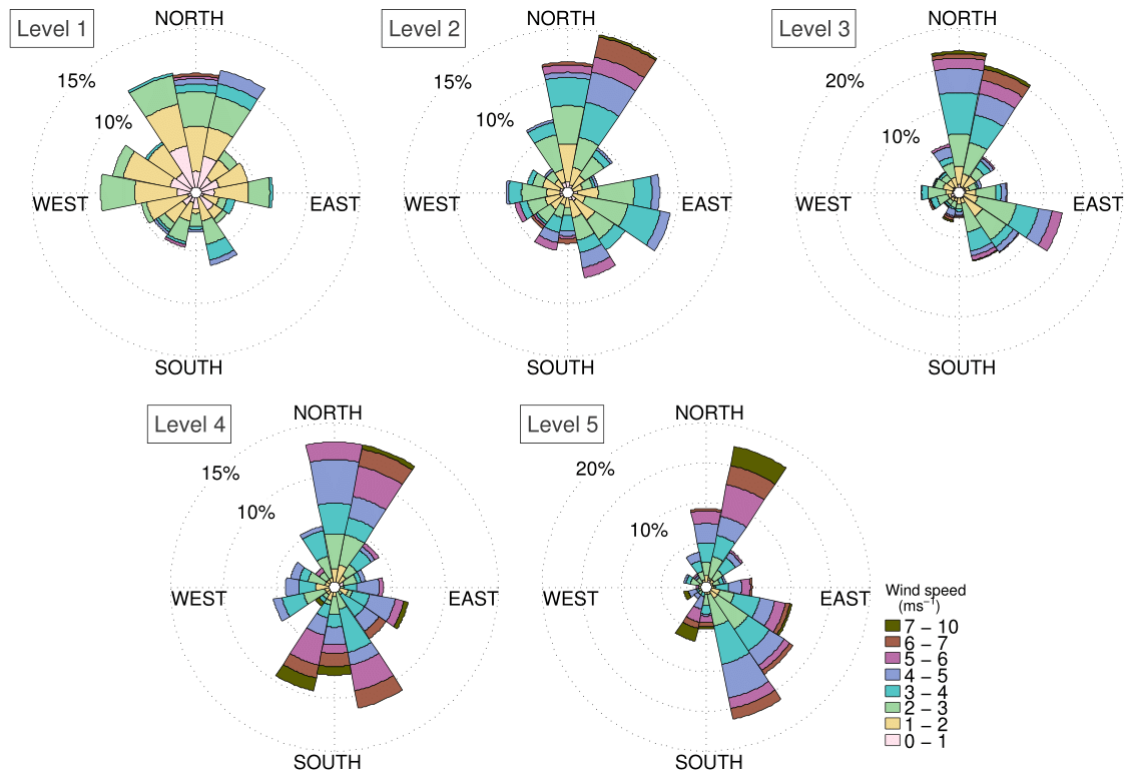
276

### 277 3.2. Post processing of the data

278 Instruments were mounted 3 m away from the triangular lattice tower (booms facing to the northeast) to  
 279 minimize any flow distortion effect by the tower. Considerable loss of data was incurred due to intermittent

280 winter icing or temporary instrument malfunction (Table 2). During this period, light nocturnal winds were  
281 common at the site at the lowest measurement level (Fig. 3). We assume that the sonic temperature  $T_s =$   
282  $T(1 + 0.51q)$ , where  $T$  is the air temperature, is close to the virtual potential temperature  $\theta_v$ . Automated  
283 quality control procedures were not used since they may be too strict for the SBL analysis of weak  
284 turbulence. Raw 20-Hz data were first divided into 30-min intervals. These intervals were checked for large  
285 data gaps, and all 30-min intervals with more than 1% of missing data were omitted from further analyses.  
286 After the consistency limits check, where we removed the data having unrealistically high values, spikes  
287 (defined as data points within the time series which deviate more than four standard deviations from the  
288 median value of the particular 30-min averaging window) were removed. If the number of spikes within the  
289 30-min interval was less than 1% of the total data, spikes were replaced by linear interpolation from  
290 neighboring values. We calculated angles of attack for each measurement and for each flux averaging  
291 period, and flagged it if angles of attack exceeded 15 deg. The number of 30-min intervals available for the  
292 further post-processing is labeled as “minimum QC” (Table 2). A cross-correlation correction of the time  
293 series is already implemented in the Gill Instruments software.

294 Although double rotation of the data is the most commonly used to correct for sonic misalignment,  
295 according to Mahrt (2011) and Mahrt et al. (2013) it should not be applied to SBL data under weak-wind  
296 conditions. In the very stable boundary layer direction-dependent mean vertical motions may occur where  
297 minor surface obstacles can significantly perturb the flow. In a setup like ours characterized by tall  
298 vegetation and/or complex terrain, a non-zero 30-min mean vertical wind component may exist. In such  
299 situations a planar fit (PF) method (Wilczak et al., 2001) would be better since it is based on an assumption  
300 that the vertical wind component is equal to zero only over longer averaging periods. PF method performs a  
301 multiple linear regression on the 30-min wind components to obtain the mean streamline plane (Aubinet et  
302 al., 2012). This plane is based on the measurements made during the 88-night period for each of five levels  
303 (Table 2).



304

305 **Fig. 3.** Wind roses at the measurement site for 30-min averaged data for the analyzed period (December  
 306 2008–February 2009). Levels 1 to 5 correspond to measurement heights of 20, 32, 40, 55 and 62 m above  
 307 the ground, respectively.

308

309 Basu et al. (2006) have shown that using an averaging window of inappropriate length can lead to false  
 310 conclusions concerning the behavior of the turbulence. In stable flows, use of an averaging time that is too  
 311 large leads to serious contamination of the computed flux by incidentally captured mesoscale motions  
 312 (Howell and Sun, 1999; Vickers and Mahrt, 2003). Previously Babić et al. (2012) applied two methods  
 313 based on Fourier analysis to determine an appropriate turbulence averaging time scale. In this study, we have  
 314 used a multiresolution flux decomposition (MFD) method (Howell and Mahrt, 1997) as described in Vickers  
 315 and Mahrt (2003). If the gap timescale is employed in the calculation of turbulent fluctuations,  
 316 contamination by mesoscale motions should be removed. Accordingly, in comparison with the use of an  
 317 arbitrary averaging time scale, similarity relationships should be improved. Here, based on the MFD method  
 318 we obtained a gap timescale of 100 sec, which is shorter than the previous value obtained by Babić et al.  
 319 (2012) for a single night case. Thus, a value of 100 sec was used here for a high-pass filtering of the time  
 320 series of raw  $u$ ,  $v$ ,  $w$  and  $T_s$  by applying a moving average. Since averaging over a longer time period (i.e. 30  
 321 or 60 min) reduces random flux errors in the case of relatively stationary turbulence, turbulent variances and

322 covariances in the present study correspond to 30-min averages. The mean wind speed and wind direction  
323 were derived from the sonic anemometer data.

324 Stationarity of the time series is a fundamental assumption of similarity theory. Thus, it should be tested  
325 prior to evaluation of similarity theory. Večenaj and De Wekker (2015) performed a comprehensive analysis  
326 to detect non-stationarity based on various tests proposed in the literature. They found that the Foken and  
327 Wichura (1996) test most often detects the largest number of non-stationary time intervals among all the  
328 tests investigated. They concluded that non-stationarity significantly decreases if detrending or high-pass  
329 filtering is applied, since highly non-stationarity (sub)mesoscale motions are removed by filtering.  
330 Therefore, while testing non-stationarity of our datasets we first removed the linear trend for each 30-min  
331 interval and then applied the Foken and Wichura (1996) test to the filtered time series. The percentage of  
332 non-stationary periods for our dataset over heterogeneous terrain in the SBL varied between 20 and 30 %  
333 depending on the level of observation (Table 2). This is slightly lower compared to studies of complex  
334 mountainous terrain of Večenaj and De Wekker (2015) and Stiperski and Rotach (2016).

335 The statistical uncertainty (or sampling error) is inherent to every turbulence measurement. The  
336 assessment of the statistical uncertainty is related to the averaging period. In order to estimate statistical  
337 uncertainty we followed Stiperski and Rotach (2016). We performed this test on the time intervals which  
338 were declared stationary by the foregoing test. The statistical uncertainty was estimated for the momentum  
339 and heat fluxes, and for the variances. This was done for the fixed averaging period of 30-min. Although  
340 over ideally flat and homogeneous surfaces one might choose 20% as a limit of statistical uncertainty, we  
341 chose the 50% to assure both, high quality data sets, and a significantly large amount of input data for the  
342 similarity analysis (Stiperski and Rotach, 2016). Thus, for the subsequent analysis only 30-min intervals  
343 associated with statistical uncertainty below 50% were chosen. The uncertainty was largest for the kinematic  
344 heat flux while for variances it was on average smaller than 50%.

345 Finally, following the QC recommendations by e.g. Klipp and Mahrt (2004) and Grachev et al. (2014)  
346 we imposed the following thresholds: data with the local wind speed less than  $0.2 \text{ ms}^{-1}$  were omitted, while  
347 minimum thresholds for the kinematic momentum flux, kinematic heat flux, and standard deviation of each  
348 wind speed component were  $0.001 \text{ ms}^{-1}$ ,  $0.001 \text{ Kms}^{-1}$  and  $0.04 \text{ ms}^{-1}$ , respectively.

349  
350

351 **Table 2**

352 Number of 30-min intervals that satisfy the minimum QC (no large data gaps, no unrealistic values and no  
 353 spikes) within the observed period of 88 nights (out of a total of 2112 possible intervals). The number of  
 354 stationary and also the number of time intervals which are stationary and have uncertainty < 50% (used for  
 355 the analysis in this study) is given.

<b>Crtieria</b>	<b>Level 1</b>	<b>Level 2</b>	<b>Level 3</b>	<b>Level 4</b>	<b>Level 5</b>
<b>Minimum QC</b>	647	802	1898	564	803
<b>Stationary</b>	482	576	1323	388	649
<b>Stationary &amp; Uncertainty &lt; 50%</b>	342	388	760	225	357

356  
 357

358 Footprints are estimated and used in order to facilitate an interpretation of the results. Kljun et al. (2015)  
 359 presented a new parameterization for Flux Footprint Prediction (FFP) which has improved footprint  
 360 predictions for elevated measurement heights in stable stratification. Furthermore, the effect of the surface  
 361 roughness has been implemented into the scaling approach. It is based on a scaling approach of flux  
 362 footprint results of a thoroughly tested Lagrangian footprint model. A two-dimensional flux footprint model  
 363 of Kljun et al. (2015) (<http://footprint.kljun.net/>) was used to estimate the surface upwind of the  
 364 measurement tower that defined the fetch (flux footprint function) for the measurements at each level during  
 365 stable conditions. As input parameters we used the mean standard deviations of lateral wind component ( $\sigma_v$   
 366 = 0.40, 0.45, 0.41, 0.46 and 0.46 ms<sup>-1</sup> for levels from 1 to 5, respectively), the mean local Obukhov lengths  
 367 ( $\Lambda = 33, 28, 38, 45$  and 39 m), the mean friction velocities ( $u_{*l} = 0.23, 0.20, 0.19, 0.22$  and 0.21 ms<sup>-1</sup>) and  
 368 correspondingly, mean wind velocity for each measurement height ( $U = 1.9, 2.9, 3.1, 4.0$  and 4.1 ms<sup>-1</sup>). The  
 369 height of the SBL was set to 250 m since the result did not exhibit noticeable sensitivity to its choice. The  
 370 peak location of the footprint function, i.e. location of the maximum influence on the measurement,  
 371 increases with increasing height and varies between 19 and 405 m from the lowest to the highest  
 372 observational level, respectively. Additionally, the distance from the receptor that includes 90% of the area  
 373 influencing the measurement ( $x_R$ ) increases with height, where  $x_R \approx 65, 331, 570, 1260$  and 1300 m,  
 374 correspond to levels 1 to 5, respectively.

375

### 376 3.3. *Assesment of self-correlation*

377 Monin-Obukhov as well as local similarity theory leads to self-correlation, because both predicted  
 378 variables and the predictors are functions of the same input quantities (Hicks, 1978). As an example,  
 379 prediction of  $\sigma_i/u_{*l}$  ( $i = u, v, w$ ) or  $\phi_m$  in terms of the stability parameter contains self-correlation since both



380  $\sigma_i/u_{*l}$  or  $\phi_m$  and  $\zeta$  depend on  $u_{*l}$ . To test the role of self-correlation in our dataset, we followed the  
381 approach of Mahrt (2003) as described in Klipp and Mahrt (2004), using 1000 random samples. Random  
382 datasets were created by redistributing the values of  $\sigma_u$ ,  $\sigma_v$ ,  $\sigma_w$ ,  $u_{*l}$  and  $dU/dz$  from the original dataset for  
383 each measurement level. We used threshold values  $-\overline{w'\theta'_v} > 0.001 \text{ mKs}^{-1}$  and  $dU/dz > 0.001 \text{ s}^{-1}$ , as values  
384 less than these are indistinguishable from zero. We repeated this process 1000 times and we calculated  
385 corresponding 1000 random linear-correlation coefficients between  $\sigma_i$  and  $\zeta$  and  $\phi_m$  and  $\zeta$ . The average of  
386 these 1000 random correlation coefficients,  $\langle R_{rand} \rangle$ , is a measure of self-correlation because random data no  
387 longer have any physical meaning. The difference between the squared correlation coefficient of the original  
388 dataset  $R_{data}^2$  and  $\langle R_{rand}^2 \rangle$  is proposed as a measure of the actual fraction of variance attributed to the  
389 physical process. A very small value of the linear-correlation coefficient ( $< 0.15$ ) indicates no correlation  
390 between compared variables. Mahrt (2014) stated that physical interpretation of results becomes ambiguous  
391 when the self-correlation is of the same sign as the expected physical correlation. However, this test does not  
392 seem to be appropriate for near-neutral and very stable cases ( $z$ -less limit), since  $\sigma_i/u_{*l}$  and  $\phi_m$  tend to  
393 constant values, resulting in small (or even negative) correlation coefficients (Babić et al., 2016)

394

## 395 **4. Results and Discussion**

### 396 *4.1. Flux-variance similarity*

397 Variances of wind velocity components provide important information on turbulence intensity as well as  
398 for the modeling of turbulent kinetic energy and transport. In this section we evaluate similarity of scaled  
399 standard deviations of wind velocity components. Normalized standard deviations of wind components are  
400 plotted as a function of the local stability parameter in Figs. 4 and 6. Figure 4 shows that scatter of the data  
401 (gray symbols) increases with increasing height, where standard deviations of 0.27, 0.29, 0.41, 0.36 and 0.34  
402  $\text{ms}^{-1}$  correspond to levels from 1 to 5, respectively. Note that the number of data is the largest at level 3.  
403 Moreover, after applying strict quality control criteria the scatter is substantially reduced (standard  
404 deviations in the range 0.21–0.23  $\text{ms}^{-1}$ ). This is similar to results of Babić et al. (2016), and opposed to some  
405 other studies in complex terrain (e.g. Fortuniak et al., 2013; Nadeau et al., 2013; Wood et al., 2010).  
406 Stationary data that exceed our uncertainty threshold of 50% are presented in order to show the influence of  
407 small fluxes (which are difficult to measure and hence uncertain) on the scatter of  $\sigma_w/u_{*l}$  (presented as  
408 gray symbols in Fig. 4). As seen from Fig. 4, this criterion is crucial for excluding the high values of the

409 scaled vertical wind variance in the strongly stable regime where  $z$ -less scaling should be valid. Without this  
 410 exclusion, an incorrect conclusion on the validity of  $z$ -less scaling might be drawn. In the subsequent  
 411 analysis these data are omitted and individual data as well as bin-averages in all figures correspond to data  
 412 (namely, wind variances and turbulent fluxes) which satisfy an uncertainty limit  $< 50\%$ .

413 To evaluate the similarity of the scaled standard deviations we used the relationship form (4), where  $a_i$ ,  
 414  $b_i$  and  $c_i$  ( $i = u, v, w$ ) are free fitting parameters (e.g. Wood et al., 2010). The best-fit coefficients were  
 415 obtained using a robust least-squares fit of all 30-min data (Table 3). We note that values of fitting parameter  
 416  $a_i$  (neutral limit) for all three non-dimensional velocity variances are smallest at the lowest measurement  
 417 level. Also, they are smaller than the canonical values for flat and uniform terrain ( $\sigma_u/u_* = 2.39 \pm$   
 418  $0.03, \sigma_v/u_* = 1.92 \pm 0.05, \sigma_w/u_* = 1.25 \pm 0.03$ , Panofsky and Dutton (1984)) which clearly indicates  
 419 influence of the RSL. This justifies our estimates of the vertical structure and footprints. Turbulence  
 420 characteristics and transport in this layer are determined by the presence of coherent structures which are  
 421 generated at the canopy top (e.g. Finnigan and Shaw, 2000; Shaw et al., 2006). These coherent eddies and  
 422 extra mixing are generated by the inviscid instability mechanism (Raupach et al., 1996). Values of  $a_{v,w}$  at  
 423 levels 2–5 are larger compared to the Panofsky and Dutton (1984) values for the neutral range, while the  $a_u$   
 424 value for level 2 is larger. For three other levels values are slightly smaller (Table 3). Values of  $\sigma_w/u_{*l}$   
 425 larger than 1.25 (value reported for “ideal” flat terrain) are often observed over non-uniform terrain and may  
 426 be attributed to horizontal momentum transport (Katul et al., 1995).

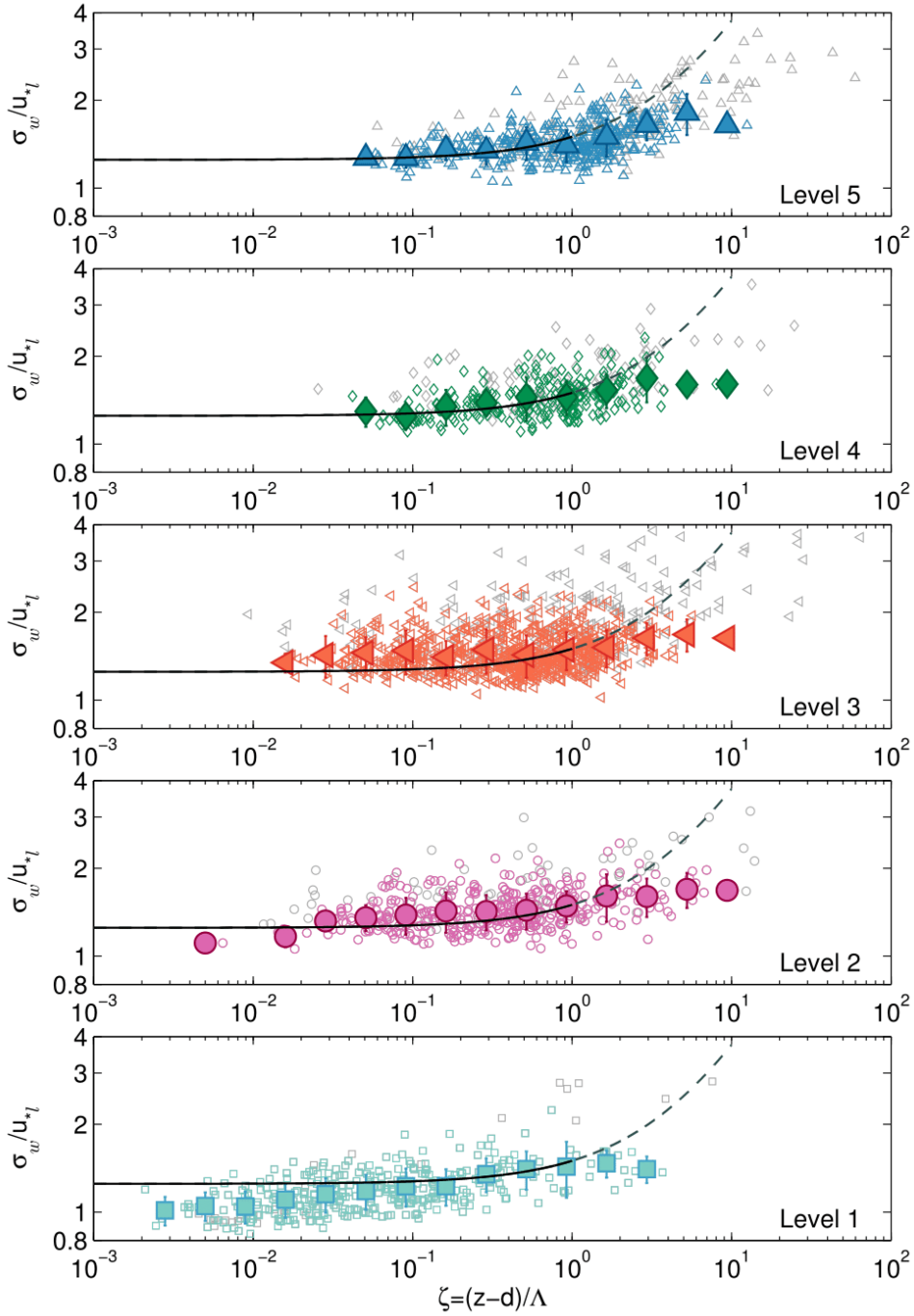
427

428 **Table 3**

429 Fitted relationships for non-dimensional standard deviations of wind components. Functional forms (Eq. (4))  
 430 of non-dimensional standard deviations of velocity components were tested using a robust least-squares  
 431 method.

Level	Height*	$\sigma_u/u_{*l}$	$\sigma_v/u_{*l}$	$\sigma_w/u_{*l}$
Level 1	20 m	$2.10(1 + 7.27\zeta)^{0.09}$	$1.30(1 + 1506\zeta)^{0.1}$	$0.94(1 + 656\zeta)^{0.06}$
Level 2	32 m	$2.48(1 + 0.57\zeta)^{0.12}$	$2.10(1 + 9\zeta)^{0.1}$	$1.34(1 + 3.39\zeta)^{0.08}$
Level 3	40 m	$2.32(1 + 0.15\zeta)^{0.36}$	$2.00(1 + 1.9\zeta)^{0.1}$	$1.43(1 + 0.18\zeta)^{0.26}$
Level 4	55 m	$2.24(1 + 0.79\zeta)^{0.15}$	$1.70(1 + 6.7\zeta)^{0.1}$	$1.21(1 + 15.94\zeta)^{0.07}$
Level 5	62 m	$2.13(1 + 0.75\zeta)^{0.17}$	$2.00(1 + 0.9\zeta)^{0.2}$	$1.30(1 + 0.59\zeta)^{0.22}$

432 \* above ground level



433

434 **Fig. 4.** Scaled standard deviation of vertical velocity fluctuations as a function of stability. Black solid line  
 435 ( $0 < \zeta < 1$ ) corresponds to:  $\phi_w = 1.25(1 + 0.2\zeta)$  (Kaimal and Finnigan, 1994). Thin dashed line is an  
 436 extension for  $1 < \zeta < 10$ . Individual data at each level are shown as background symbols (gray symbols  
 437 represent stationary data points which exceed our uncertainty threshold of 50%). Error bars indicate one  
 438 standard deviation within each bin. The bin size is determined in a logarithmic scale using fifteen equally  
 439 spaced bins in the stability range  $0.002 < \zeta < 12.5$ .

440

441 As already mentioned, flux-variance similarity relationships are influenced by self-correlation. Small  
 442 values of fitted coefficients  $b_i$  and/or  $c_i$  indicate the best-fit curve which converges to a constant, i.e.  $a_i$ .  
 443 Consequently, values of  $R_{data}^2$  tend to converge to small values or even to zero, while  $\langle R_{rand}^2 \rangle$  are usually  
 444 larger which leads to negative values of  $R_{data}^2 - \langle R_{rand}^2 \rangle$ . The same result was obtained by Babić et al.  
 445 (2016) and, as they pointed out, this presents a limitation of the method since it relies on the linear  
 446 correlation coefficient and does not allow for a reliable conclusion about self-correlation in the SBL.

447 Table 4 presents a review of  $\sigma_{u,v,w}/u_{*l}$  published in the literature for different terrain characteristics  
 448 under neutral conditions. As already noted, dimensionless velocity variances in the RSL often exhibit  
 449 lower values in comparison with the flat terrain reference of Kaimal and Finnigan (1994). Our results for  
 450  $\sigma_{u,v}/u_{*l}$  at the lowest measurement level are in the range of values obtained within RSLs over forest  
 451 (Rannik, 1998) and urban (Rotach, 1993) areas. For levels 2–5, neutral values are close to those reported  
 452 by Moraes et al. (2005) and Wood et al. (2010). Using local scaling over the city of London  
 453 (measurements at 190 m above the ground), Wood et al. (2010) obtained near-neutral limits of  $\sigma_i/u_{*l}$   
 454 ( $i = u, v, w$ ), which are in accordance with those reported for flat and homogeneous terrain where MOST  
 455 applies. They concluded that MOST was not complicated by too many factors, since London is quite flat  
 456 and there are consistent building heights across a wide area which produced a longer upwind fetch causing  
 457 the London boundary layer likely to be in equilibrium with the surface. Our results for  $\sigma_w/u_{*l}$  are  
 458 furthermore consistent with Nieuwstadt (1984) who found it to be constant ( $\sim 1.4$ ) in the stability range  
 459  $0.1 < \zeta < 2$ .

460 **Table 4**

461 Comparison of neutral values for non-dimensional standard deviations of the wind from different studies.  
 462 Our near-neutral values correspond to the mean value of scaled standard deviations of wind in the range  
 463  $0 < \zeta < 0.05$ .

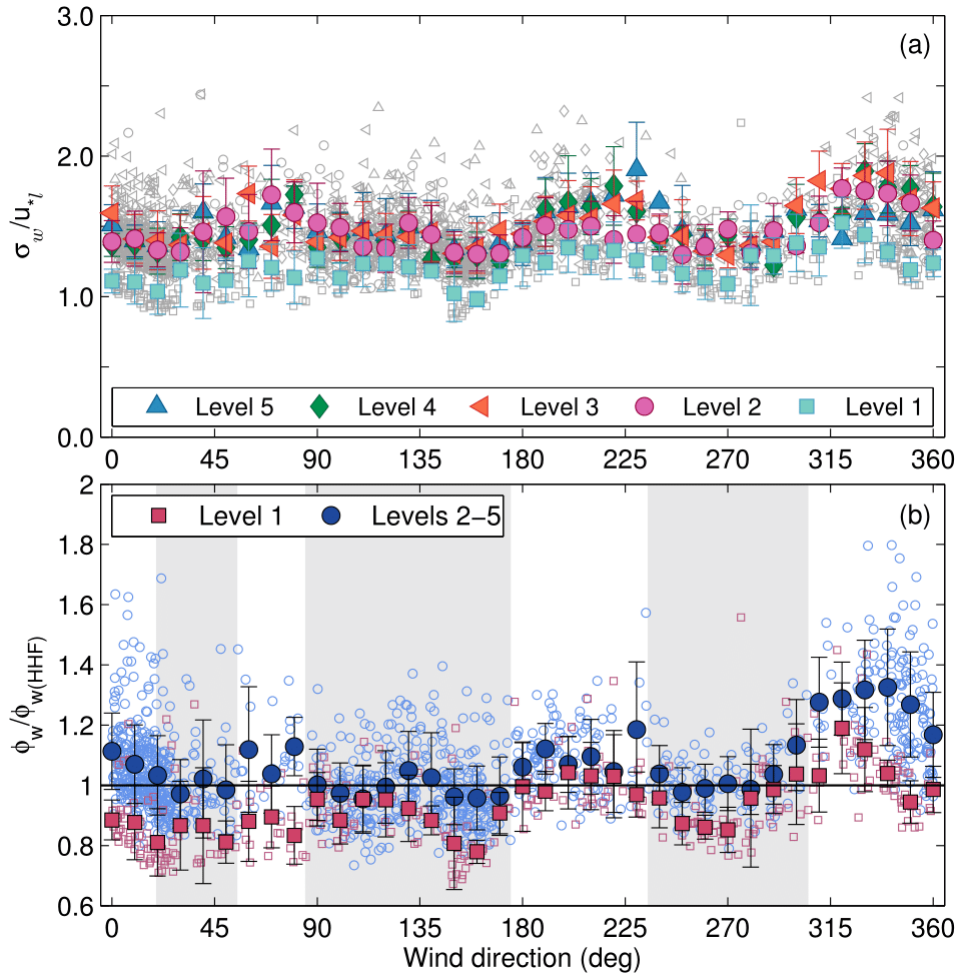
Reference	Site description	$\sigma_u/u_{*l}$	$\sigma_v/u_{*l}$	$\sigma_w/u_{*l}$
Panofsky and Dutton (1984)	Flat (reference)	$2.39 \pm 0.03$	$1.92 \pm 0.05$	$1.25 \pm 0.03$
Rotach (1993)	Urban RSL	2.2	1.5	0.94
Rannik (1998)	Pine forest RSL	$2.25 \pm 0.31$	$1.82 \pm 0.29$	$1.33 \pm 0.14$
Moraes et al. (2005)	Complex (valley)	2.4	2.2	1.2
Wood et al. (2010)	Urban BL	2.36	1.92	1.40
This study – Level 1	Heterogeneous	2.13	1.65	1.11
This study – Levels 2–5	Heterogeneous	2.41	2.08	1.37

464

465 4.1.1. *Influence of the surface heterogeneity*

466 Due to the fact that measurements were performed in a very heterogeneous landscape, we investigated  
467 possible influences of different land-use types on turbulence statistics by considering changes for different  
468 wind directions. Figure 5a shows the normalized standard deviation of the vertical wind component for each  
469 observational level averaged over the entire stability range plotted versus wind direction. For the wind sector  
470 45–90 deg there is no consistent increase of  $\sigma_w/u_{*l}$  with height, possibly due to the fact that this narrow  
471 wind sector is characterized through a sudden change of surface roughness (from agricultural fields to rough  
472 forest) and also through a short fetch (some 70 m). This might indicate a more complex vertical structure  
473 than depicted in Fig. 2 with flow which has not reached equilibrium yet. In the 300–360 deg wind sector,  
474 the non-dimensional variance of the vertical wind has decreased values at the highest level in comparison  
475 with values at levels 2–4. We hypothesize that this might indicate an influence of drainage flows from hills  
476 located north of the measurement site. Drainage flows are thermally-driven and they occur during night over  
477 sloping terrain often leading to the formation of low level jets. However, we do not have the necessary  
478 information to substantiate this hypothesis. In the 190–260 deg sector,  $\sigma_w/u_{*l}$  increases with height  
479 indicating the flow which has adjusted to the new surface. This sector has the longest fetch (over 300 m) and  
480 highly rough but uniform underlying surface (Figs. 1 and 2).

481 Observed changes of the normalized vertical wind variance with varying wind direction reflect the  
482 influence of the surface inhomogeneity (and possibly topography). This influence is seen from the ratio of  
483 observed non-dimensional variance of the vertical wind and corresponding values of commonly used  
484 similarity formulas for  $\sigma_w/u_{*l}$  in the “ideal” HHF terrain (e.g. Kaimal and Finnigan (1994),  $\sigma_w/u_{*l} = 1.25(1$   
485  $+ 0.2\zeta)$ ) in the stability range  $0 < \zeta < 1$  (Fig. 5b). We observe that ratio of these two similarity functions at  
486 the lowest measurement level is typically less than one, except for the flow from sectors 200–220 deg and  
487 300–340 deg, which correspond to high roughness and long fetch (Fig. 1) and high wind speeds (Fig. 3),  
488 respectively. At upper levels values of the ratio  $\phi_w/\phi_{w(HHF)}$  are larger than unity for wind azimuth ranges  
489 55–80 deg, 170–230 deg and 300–360 deg (Fig. 5b). For these levels, the average  $\phi_w/\phi_{w(HHF)}$  ratio in  
490 Fig. 5b varies between 0.96 and 1.33, which is similar to values obtained by Rannik (1998) in the study over  
491 a forest, and the standard deviation for 10 deg wide bins is between 0.08 and 0.22.



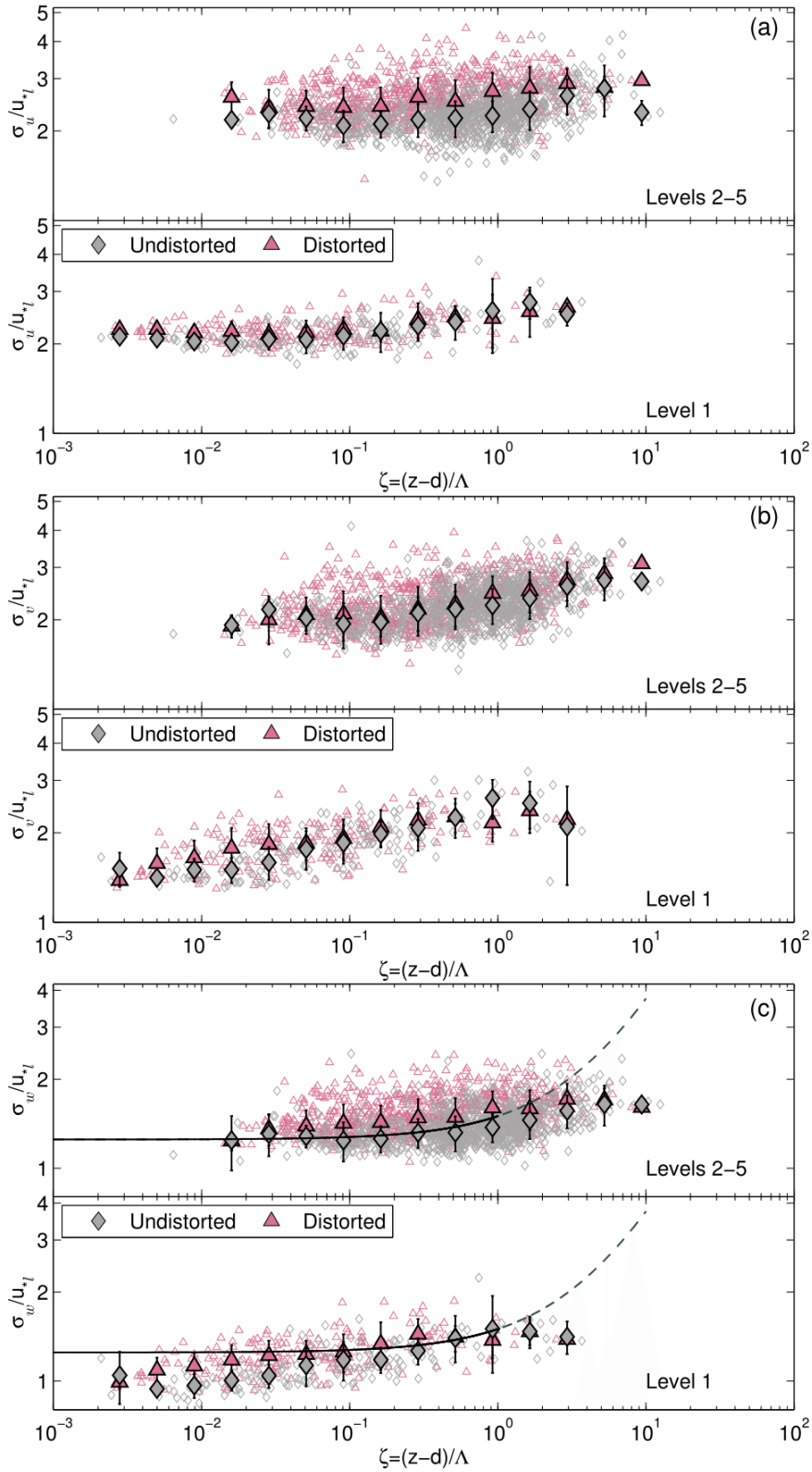
492

493 **Fig. 5.** (a) Scaled standard deviation of vertical velocity fluctuations as a function of wind direction  
 494 (regardless of stability). Individual data points at each level corresponding to the particular wind sector are  
 495 shown as background symbols. Colored filled symbols correspond to bin averages over the entire stability  
 496 range at each observational level. Error bars indicate one standard deviation within each bin. (b) Observed  
 497 dimensionless standard deviation of vertical wind speed (for the lowest level and levels 2–5) relative to the  
 498 SL similarity prediction for HHF terrain (Kaimal and Finnigan (1994), denoted “HHF”) for stability  $0 < \zeta <$   
 499  $1$ , plotted versus wind direction. Shaded light gray areas indicate the wind azimuths which correspond to  
 500 undistorted surface conditions ( $\phi_w / \phi_{w(HHF)} \approx 1$ ). These correspond to wind directions 20–55 deg, 85–175  
 501 deg and 235–295 deg. The flow from other wind directions is considered as distorted.

502

503 Accordingly, we separately analyzed the velocity variances for different wind directions corresponding  
 504 to undistorted and distorted sectors, respectively. Based on  $\phi_w / \phi_{w(HHF)} \approx 1$  undistorted wind directions  
 505 were defined to correspond to wind directions 20–55 deg, 85–175 deg and 235–295 deg (light gray shaded  
 506 area in Fig. 5b). All other wind directions were considered as distorted. The number of data within each  
 507 group was nearly evenly distributed except for the highest level. Namely, the percentage of data  
 508 corresponding to the undistorted sectors was 47, 56, 54, 52 and 64 % for levels from 1 to 5, respectively.

509 Figure 6 shows all three non-dimensional standard deviations at the lowest level and for levels 2–5 for  
510 undistorted and distorted wind direction sectors separately. We note that the scatter is larger for horizontal  
511 components than for the vertical wind component. Also, as one might expect the scatter is larger for the  
512 distorted sectors compared to undistorted. Normalized variances at level 1 show much less dependence on  
513 the wind direction compared to levels 2–5. This reflects the rather local RSL impact that determines the  
514 statistics. That is, RSL turbulence appears to be affected by a fetch of less than 100 m from the tower as was  
515 estimated by the flux-footprint model (Section 3.2.) rather than by the more distant complex surface.  
516 Differences between distorted and undistorted sectors at this level are only found in the near-neutral regime  
517 with larger magnitudes for the distorted sectors. For levels 2–5 we observe that the overall shape of the  
518 curves for the two sectors is quite similar for all three wind variances. Dimensionless longitudinal and  
519 vertical wind variances show higher values in the distorted sectors, while the lateral wind variance seems to  
520 be independent on the wind direction. Similar to level 1, the lateral wind component shows a more  
521 pronounced increase with stability than the longitudinal and vertical variances. The dimensionless vertical  
522 wind variance in the undistorted sectors can be represented quite well with the similarity relationship valid  
523 for flat and homogeneous terrain (Kaimal and Finnigan, 1994) in the stability range  $0.01 < \zeta < 1$ . Based on  
524 modeled footprints particular wind sectors were related to corresponding surface types, accordingly. For the  
525 undistorted wind directions 20–55 deg and 85–175 deg the underlying surface is represented with  
526 agricultural fields, while the 235–295 deg sector represents somewhat rougher but quite uniform surface  
527 covered mostly with the forest (Fig. 1). This implies that measurements at levels 2–5 corresponding to these  
528 sectors correspond to a layer which is in equilibrium with the underlying surface of more uniform roughness.  
529 In the strongly stable regime (for  $\zeta > 1$ ) the normalized variances show a tendency for a leveling-off, thus  
530 suggesting that  $z$ -less scaling might be appropriate. This implies that even for highly inhomogeneous terrain  
531 local scaling appears to be appropriate for all three velocity variances and that the local Obukhov length is  
532 relevant length scale. Additionally, in the strong stability limit the  $z$ -less scaling seems to be appropriate for  
533 longitudinal and vertical wind variances.



534

535 **Fig. 6.** Scaled standard deviations of (a) longitudinal, (b) lateral and (c) vertical velocity fluctuations as  
 536 functions of stability for level 1 (lower sub-panels) and levels 2–5 (upper sub-panels) for distorted (pink  
 537 triangles) and undistorted (gray diamonds) wind sectors. For explanation of other symbols see Fig. 4.  
 538

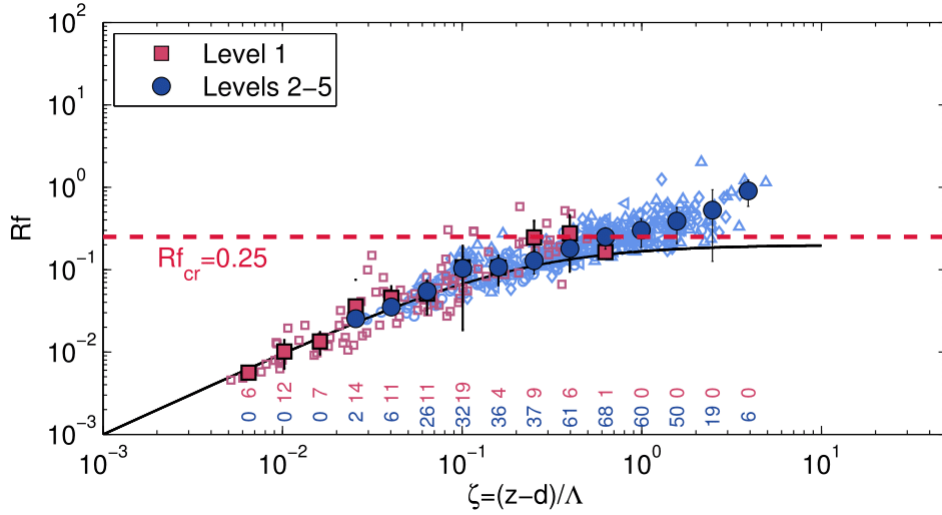


539 4.1.2. *Subcritical and supercritical turbulence regimes*

540 Grachev et al. (2013) showed that the inertial subrange, associated with the Richardson-Kolmogorov  
541 cascade, dies out when both the gradient and the flux Richardson number exceed a “critical value” of  
542 approximately 0.20 – 0.25, with  $Rf_{cr} = 0.20 - 0.25$  being the primary threshold. They argued that a  
543 collapse of the inertial subrange is caused by the collapse of energy-containing/flux-carrying eddies. This  
544 leads to the invalidity of Kaimal's spectral and cospectral similarity (Kaimal, 1973) and consequently, to  
545 violations of flux-profile and flux-variance similarity. Correspondingly, Grachev et al. (2013) classified the  
546 traditional SBL into two major regimes: subcritical and supercritical. In the former ( $Ri < Ri_{cr}$  and  $Rf <$   
547  $Rf_{cr}$ ), turbulence statistics can be described by similarity theory and it is associated with Kolmogorov  
548 turbulence. The supercritical regime ( $Ri > Ri_{cr}$  and  $Rf > Rf_{cr}$ ) is related to small-scale, decaying, non-  
549 Kolmogorov turbulence, and strong influence of the Earth's rotation even near the surface. Figure 7 shows  
550 the dependence of  $Rf$  (Eq. (8)) on the local stability parameter at the measuring site. Dyer's parameterization  
551 (Dyer, 1974) predicts an asymptotic limit to  $Rf_{cr} = 0.2$  (solid black line), but this under-predicts  $Rf$  for  
552 higher stabilities for which  $Rf$  increases above  $Rf_{cr} = 0.25$  (supercritical regime). The range of stability  
553 available for our analysis of the profile data is  $0 < \zeta < 5$ . For example, at levels 4 and 5, 40% and 50% of  
554 data points have  $Rf > Rf_{cr}$ , respectively. Thus, higher levels, which correspond to higher stabilities, are  
555 characterized by non-Kolmogorov turbulence.

556 Grachev et al. (2013) have found that  $Rf_{cr} = 0.20$  was the primary threshold for  $\sigma_w/u_{*l}$ . The  
557 normalized standard deviation of the vertical wind speed was reported to become asymptotically constant in  
558 the subcritical regime indicating consistency with  $z$ -less scaling in this regime. In the supercritical regime  
559  $\sigma_w/u_{*l}$  was monotonically increasing with increasing stability. The turbulence characteristics at our site  
560 (exemplified by the vertical velocity variance, Fig. 8) do not show a clear distinction in behavior between  
561 sub- and supercritical regimes as was found in Grachev et al. (2013) and for the non-dimensional vertical  
562 gradient of mean wind (Fig. 12). In the subcritical regime the number of data points at levels 2–5 with  $\zeta > 1$   
563 is equal to 25 and is represented by only two bin averages. While Grachev et al. (2013) had a much broader  
564 range of stability in both regimes (they obtained  $z/\Lambda$  as small as 0.02 for the supercritical and up to 5 for the  
565 subcritical regime, respectively), in our dataset the results for these two regimes are almost indistinguishable  
566 (Fig. 8). Additionally, for the supercritical regime Grachev et al. (2013) observed an

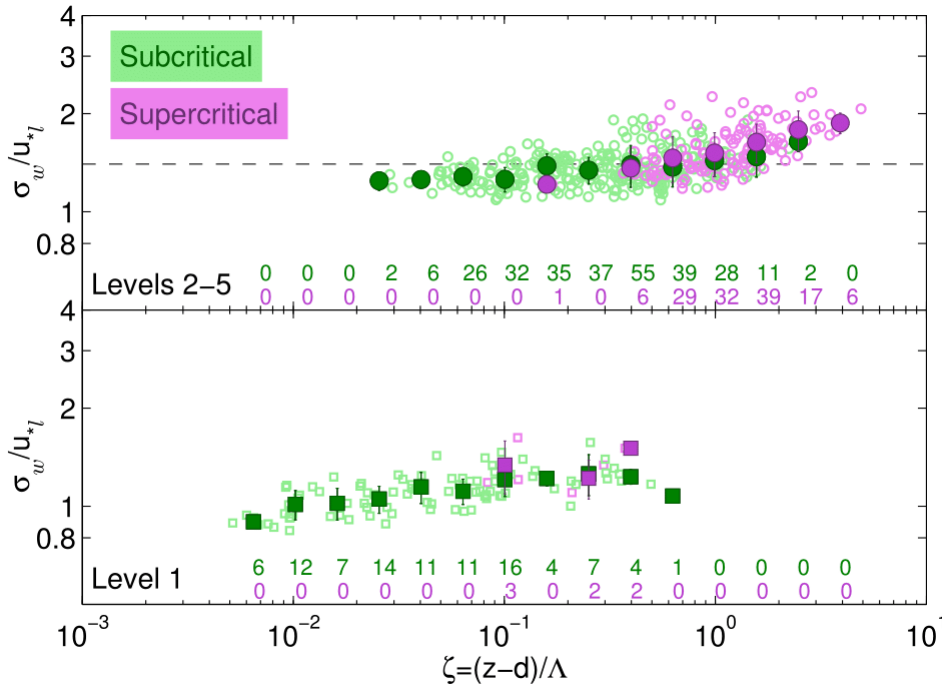
567



568

569 **Fig. 7.** Stability dependence of the flux Richardson number for all five levels (shown with corresponding  
 570 symbol). Red squares and blue circles denote bin averages for the lowest level and for levels 2–5,  
 571 respectively. Error bars indicate one standard deviation within each bin. Number of data points inside each  
 572 bin for the two subsets of the data is also given.

573



574

575 **Fig. 8.** Scaled standard deviation of vertical velocity fluctuations as a function of stability. Data from the  
 576 lowermost level (squares) and for levels 2–5 (circles) in the subcritical (green) and supercritical (violet)  
 577 regime are presented. The dashed line is equal to 1.4 which is the mean value of all data for levels 2–5 in the  
 578 subcritical regime. The number of data in each regime is indicated with the corresponding color.

579

580 increase of  $\sigma_w/u_{*l}$  in the range  $3 < \zeta < 100$ . For this regime we observed an increasing tendency for the two  
 581 highest levels, but this is probably not significant because of the small number of data and a restricted

582 stability range (upper limit is  $\zeta = 5$ ). Note that the number of data points here is much less compared to Figs.  
 583 4 and 6 because only 100 simultaneous 30-min intervals were available for the calculation of the flux  
 584 Richardson number. Similar results are found for the horizontal wind variances (not shown).

585

#### 586 4.2. Turbulent kinetic energy

587 Estimation of turbulent kinetic energy (TKE) is very important for atmospheric numerical modeling,  
 588 since turbulent mixing is often parameterized using TKE. Here we investigate the TKE, defined as,  $e =$   
 589  $\frac{1}{2}(\overline{u'^2} + \overline{v'^2} + \overline{w'^2})$ , which represents a turbulent kinetic energy per unit mass (Stull, 1988). Fig. 9 shows  $e$   
 590 scaled by the squared friction velocity. In numerical models which use 1.5-order closure or TKE closure,  
 591 TKE is predicted with a prognostic energy equation, and eddy viscosity is specified using the TKE and some  
 592 length scale. Since TKE is essentially the sum of variances (divided by 2), according to Kansas values for  
 593 neutral conditions (Kaimal and Finnigan, 1994), the value of scaled TKE is equal to 5.48 for HHF terrain.

594 Over HHF terrain in Antarctica, Sanz Rodrigo and Anderson (2013) found that for neutral to moderate  
 595 stabilities non-dimensional TKE is roughly constant up to  $\zeta = 0.5$ . Above this value, non-dimensional TKE  
 596 grows until it reaches  $\zeta = 10$  (corresponding to the boundary-layer top), which is followed by an asymptotic  
 597 value for stronger stabilities (Fig. 9, dashed black line, Eq. (14)). They proposed a simple empirical  
 598 parameterization:

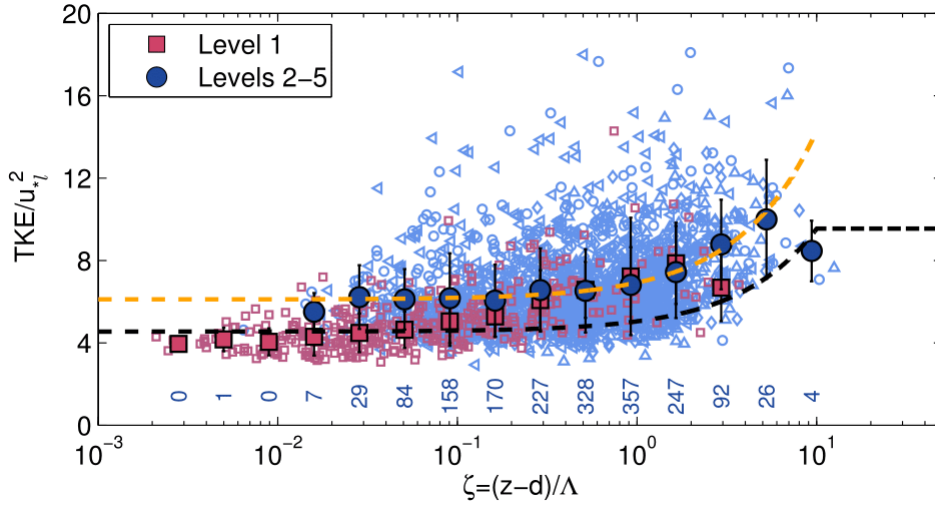
$$\frac{TKE}{u_{*l}^2}(\zeta) = \begin{cases} \frac{1}{\alpha_0} + b_E \zeta, & \zeta \leq 10 \\ \frac{1}{\alpha_0} + b_E 10, & \zeta > 10 \end{cases} \quad (14)$$

599 where  $\alpha_0 = 0.22$  is the neutral limit value and  $b_E = 0.5$ .

600 We fitted the above linear relation to our data from levels 2–5 in the stability range  $0.006 < \zeta < 8.30$   
 601 (Fig. 9, orange dashed line) using the least-squares method. Figure 9 shows a clear influence of the RSL on  
 602 the lowest measurement level, which does not correspond to the proposed near-linear expression (14). The  
 603 RSL influence also results in a reduced value of non-dimensional TKE for the neutral range ( $TKE/u_{*l}^2 \approx$   
 604 4.25 based on values from Tab. 4) in comparison with the value of 4.5 found by Sanz Rodrigo and Anderson  
 605 (2013). Their value is smaller than the reference value of 5.48 for HHF terrain probably due to higher air  
 606 density in the Antarctica causing reduced values of  $TKE/u_*^2$  compared to mid-latitudes. We note that the  
 607 relation of the type given by Eq. (14) fits our data for levels 2–5 quite well (Fig. 9, orange dashed curve),

608 but with slightly different coefficients  $\alpha_0 = 0.16$ , which corresponds to a neutral value of  $TKE/u_*^2 = 6.1$ ,  
 609 and  $b_E = 0.8$ . The fitted neutral value of dimensionless TKE for levels 2–5 is close to the value of 6.01,  
 610 which is obtained based on values from Tab. 4.

611



612

613 **Fig. 9.** Dependence of non-dimensional turbulent kinetic energy on stability. The black dashed line is an  
 614 empirical fit (Eq. (14), Sanz Rodrigo and Anderson (2013)). Individual data at each level are shown in  
 615 background symbols, while red squares and blue circles represent bin-averages for the lowest and four  
 616 higher levels, respectively. Error bars indicate one standard deviation within each bin. The number of data  
 617 points within each bin for levels 2–5 is also indicated. The orange curve is a fit to our data for levels 2–5.

618

619 Similar to wind variances, analysis of the TKE with respect to wind direction shows similar distinction  
 620 between the distorted and undistorted sectors. While values of normalized TKE are similar for the two  
 621 sectors at the lowest level, at levels 2–5 magnitudes in the distorted sectors are larger. The dependence of  
 622  $TKE/u_*^2$  on the stability parameter can be represented with a linear relationship, but the best fit coefficients  
 623 are somewhat changed:  $\alpha_0 = 0.19$  and  $0.14$  and  $b_E = 0.97$  and  $0.95$  for undistorted and distorted sectors,  
 624 respectively (not shown). The behavior of the normalized TKE in the sub- and supercritical regime was  
 625 found to be consistent with the behavior of the normalized wind variances and no discernible difference  
 626 between these two regimes was observed (not shown).

627 4.3. Correlation coefficients

628 In order to estimate fluxes from mean wind and temperature as inputs for dispersion models it is useful  
 629 to use turbulent correlation coefficients. These coefficients are a measure of the efficiency of turbulent  
 630 transfer and are defined as

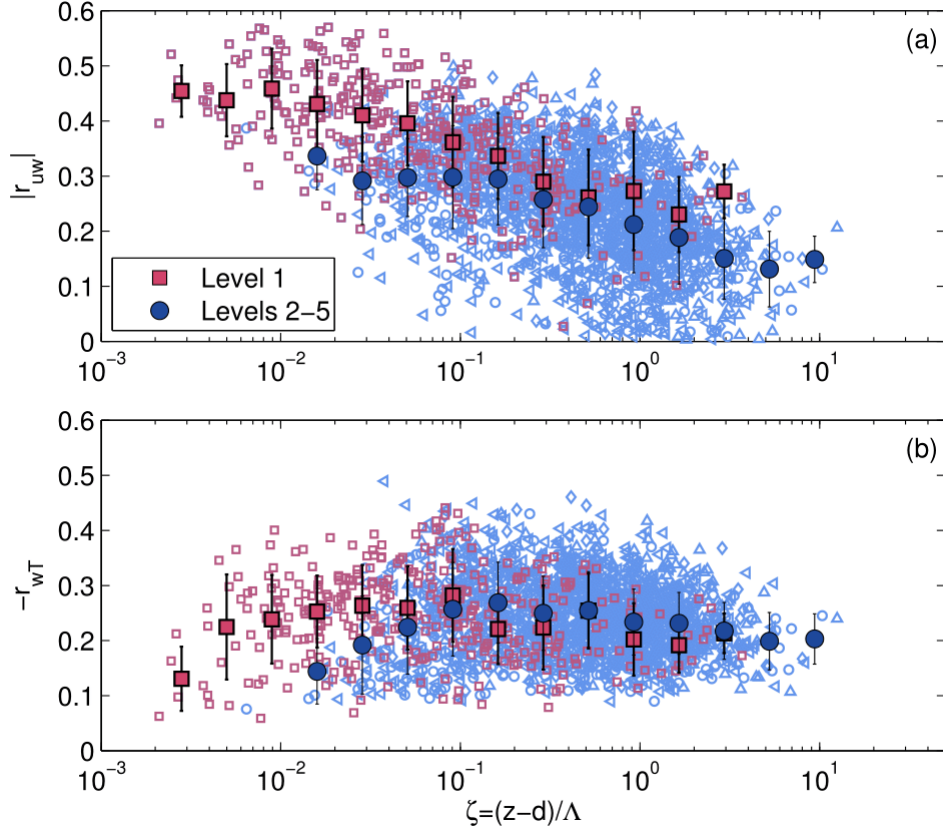
$$r_{uw} = \frac{\overline{u'w'}}{\sigma_u \sigma_w} \quad (15)$$

$$-r_{wT} = \frac{\overline{w'\theta'_v}}{\sigma_w \sigma_{\theta_v}} \quad (16)$$

631 where  $r_{uw}$  and  $r_{wT}$  are correlation coefficients for momentum and heat transfer, respectively. Figure 10  
 632 shows momentum and heat flux correlation coefficients estimated for the lowest and the four higher  
 633 measurement levels. For strong stratification we obtained smaller values of the correlation coefficients for  
 634 momentum, but they increase quite steeply while approaching neutral conditions. This was also observed in  
 635 both an urban (e.g. Wood et al., 2010) and a rural dataset (e.g. Conangla et al., 2008). Additionally,  $r_{uw}$   
 636 exhibits the same behavior with respect to the stability when analyzed for different wind azimuths. The  
 637 magnitude of the momentum correlation coefficient is larger for the undistorted sector compared to distorted  
 638 in the stability range  $0 < \zeta < 1$  in the whole measurement layer (not shown). The stability-averaged  
 639 momentum flux correlation coefficient values are between 0.23 and 0.46 at level 1 (Fig. 10a) and a similar  
 640 range was observed for undistorted (0.22–0.51) and distorted (0.25–0.45) wind sectors. These values are  
 641 similar to those obtained by Marques Filho et al. (2008). For levels 2–5, the values of  $r_{uw}$  are somewhat  
 642 smaller compared to level 1 and are in the range 0.14–0.34 (Fig. 10a), and they are similar to those obtained  
 643 for the distorted wind sectors: 0.16–0.31 (not shown), which is in the range of values observed over  
 644 generally rougher urban surfaces (Wood et al., 2010).

645 The correlation coefficient for heat exhibits larger values for  $\zeta > 0.1$  for levels 2–5, and it decreases  
 646 while approaching neutral conditions. The correlation coefficient for heat is between 0.10 and 0.26, which is  
 647 similar to values reported in other studies (Marques Filho et al., 2008; Wood et al., 2010). Additionally, no  
 648 discernible dependence on wind direction was found for  $r_{wT}$  mostly due to the large scatter of the data (not  
 649 shown). Mean values of the momentum and heat flux correlation coefficients over the entire measurement  
 650 layer, and for all stabilities, are equal to 0.26 and 0.24, respectively. Also, no discernible difference in

651 behavior of the momentum and heat flux correlation coefficients was observed between the sub- and  
 652 supercritical regimes (not shown).  
 653



654  
 655 **Fig. 10.** Momentum (a) and heat flux (b) correlation coefficients plotted as a function of stability.  
 656 Background symbols represent individual data at each level while red squares and blue circles show bin-  
 657 averages for the first level and for levels 2–5, respectively. Error bars indicate one standard deviation  
 658 corresponding to the particular bin.

659  
 660 *4.4. Flux-gradient similarity*

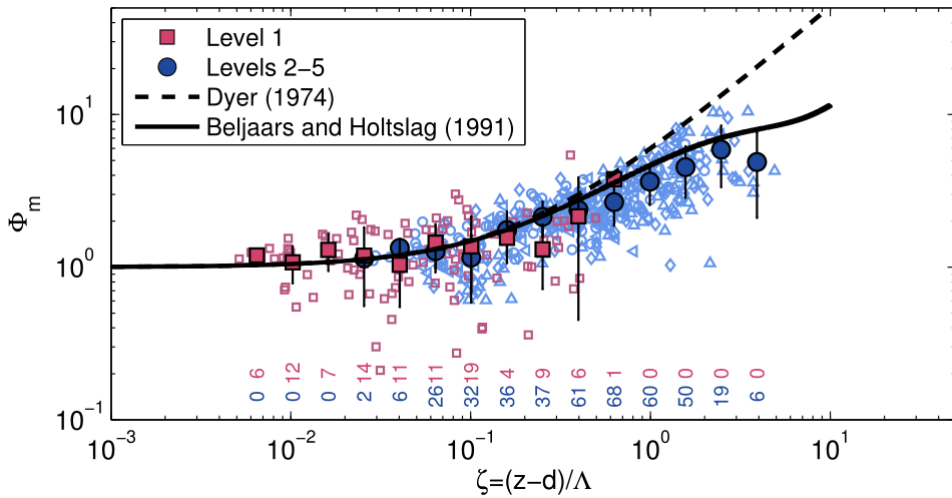
661 We also investigated the relationship between mean vertical gradients and turbulent fluxes, also known  
 662 as the flux-gradient relationships. Several interpolation methods were tested in order to determine the mean  
 663 wind profile, and the second order polynomial fit was found to best fit the observed data. Thus, the vertical  
 664 gradient of mean wind speed is obtained by fitting a second order polynomial through the 30-min measured  
 665 profiles

$$U(z) = p_1 \left[ \ln \left( \frac{z-d}{z_0} \right) \right]^2 + p_2 \ln \left( \frac{z-d}{z_0} \right) + p_3 \quad (17)$$

666 and by evaluating a derivative with respect to  $z$  for each measurement level. The second order polynomial fit  
667 is widely used for measurements within the roughness sublayer (e.g. Dellwik and Jensen, 2005; Rotach,  
668 1993) as well as within the inertial sublayer (e.g. Forrer and Rotach, 1997; Grachev et al., 2013). Only about  
669 one hundred simultaneous 30-min intervals were available from each measurement level for the profile  
670 analysis. Results of the variance and TKE analyses showed a different behavior of the first level in  
671 comparison with all the others. In order to investigate whether there is a difference in the flux-gradient  
672 relationship as well, the data from the first level and levels 2–5 are presented separately (Fig. 11). For our  
673 dataset no discernible difference of  $\phi_m$  between level 1 and levels 2–5 can be observed. Almost all data at  
674 the first measurement level are within the stability range  $z/\Lambda < 0.5$  and  $\phi_m$  tends to a constant value of 1  
675 when approaching near-neutral conditions. Quite diverse results concerning the value of  $\phi_m$  in the RSL in  
676 the near-neutral conditions can be found in the literature. While in some studies of flux-gradient similarity  
677 within the forest RSL,  $\phi_m$  was found to be less than unity in the near-neutral range (e.g. Högström et al.,  
678 1989; Mölder et al., 1999; Raupach, 1979; Thom et al., 1975), other studies indicate that  $\phi_m$  is close to unity  
679 (e.g. Bosveld, 1997; Simpson et al., 1998; Dellwik and Jensen, 2005; Nakamura and Mahrt, 2001). Bosveld  
680 (1997) found that momentum and heat eddy diffusivities differ in magnitude in neutral conditions. This  
681 means that, with increasing canopy density, heat exchange remains enhanced in the RSL, whereas  
682 momentum exchange approaches surface-layer values. Dellwik and Jensen (2005) observed an increase of  
683  $\phi_m$  in the RSL in neutral conditions over fetch-limited deciduous forest due to the increased wind gradients  
684 directly above the canopy top. In previous studies reporting  $\phi_m < 1$  and having mostly been conducted over  
685 pine forests (which compared to a closed deciduous forest have less biomass in the top of the canopy) the  
686 observed wind profile close to the three tops was less steep.

687 The previous sections have revealed clear differences in the flux-variance relationships between level 1 and  
688 levels 2-5 (i.e., the RSL and the transition layer, respectively) at the present site. In contrast, no significant  
689 difference is observed for the flux-gradient relationship. Similar results were reported by Katul et al. (1995)  
690 who pointed out that inhomogeneity in the RSL impacts variances but not necessarily fluxes. Following this  
691 line, our results seem to indicate that surface characteristics at our site are influencing the strength of  
692 turbulent mixing and the wind gradient in the same way. This conclusion is additionally corroborated by the  
693 results of the analysis for different wind sectors as no dependence on the wind direction was found for the  
694 non-dimensional gradient of wind speed (not shown).

695 According to Fig. 11,  $\phi_m$  increases more slowly with increasing stability than predicted by the linear  
696 approach (Eq. (6), dashed black line) and it appears to closely follow the Beljaars-Holtslag function (Eq.  
697 (7)). The Beljaars-Holtslag formulation reduces the overestimation of the non-dimensional gradients for very  
698 stable conditions (Fig. 11, black solid line). Similar results were also obtained by other studies. For example,  
699 Mahrt (2007) found that  $\phi_m$  increases linearly only up to 0.6, while in the range  $0.6 < \zeta < 1.0$  it increases  
700 more slowly than the linear prediction. However, according to Grachev et al. (2013) this result brings into  
701 question  $z$ -less scaling. Assuming that  $\phi_m$  is a linear function of stability, the gradients should tend to  
702 constant values for  $\zeta \gg 1$ . Thus, the leveling-off of the  $\phi_m$  at large stabilities is an evidence for the  
703 breakdown of  $z$ -less stratification. Grachev et al. (2013) hypothesized that the leveling-off of  $\phi_m$  functions  
704 for strong stability may be due to including data for which local similarity is not applicable into the analysis.  
705

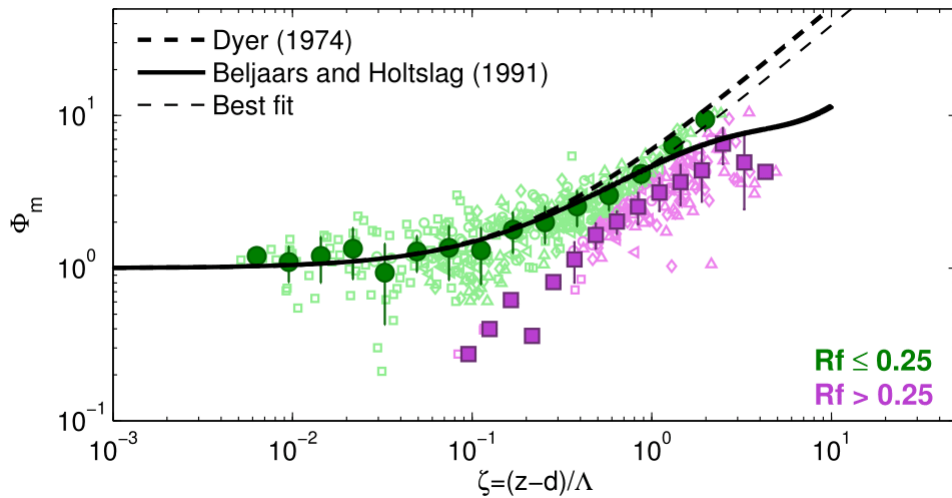


706  
707 **Fig. 11.** Non-dimensional vertical gradient of the wind speed plotted versus the local stability parameter.  
708 Individual data points for each level are shown in the corresponding symbol (as in Fig. 4), while data from  
709 the lowest level are indicated with red color and from levels 2–5 in blue color. Dashed line corresponds to  
710 the linear relationship of Dyer (1974)(Eq. (6)) and the solid line is Beljaars and Holtslag (1991) relationship  
711 (Eq. (7)). Bin averages for the lowest and four higher levels are included for easier interpretation of results.  
712 Error bars indicate one standard deviation within each bin. Number of data points in each bin is also shown.  
713

714 Following the approach of Grachev et al. (2013), we imposed the prerequisite  $Rf < Rf_{cr} = 0.25$  on all  
715 individual data at each level. According to Fig. 12, data with  $Rf < 0.25$  almost perfectly follow the linear  
716 dependence on stability (according to Eq. (6)) with the best-fit coefficient  $b_E = 3.8$  (thin dashed line in Fig.  
717 12). This implies the consistency of the data with the  $z$ -less prediction. The behavior of the non-dimensional



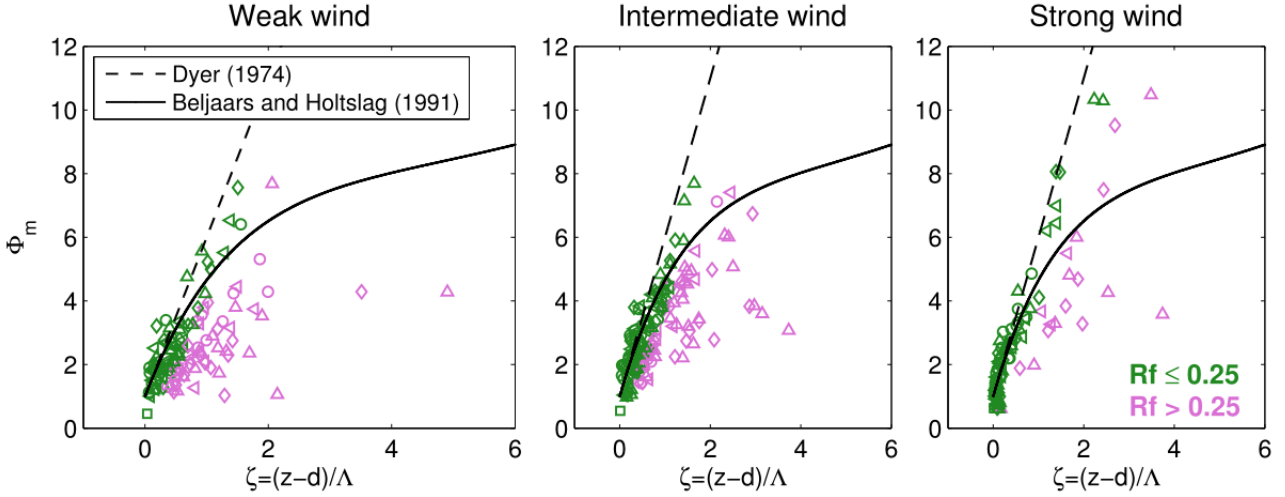
718 gradient of wind speed in the supercritical regime in Fig. 12 exhibits a large deviation from the linear  
 719 similarity prediction in the entire stability range. Moreover, supercritical data have a tendency to level-off.  
 720 This suggests that the Beljaars-Holtslag non-linear expression ( Eq. (7), Beljaars and Holtslag, 1991), as well  
 721 as the results from other studies which exhibited leveling-off of similarity functions (e.g. Baas et al., 2006;  
 722 Forrer and Rotach, 1997; Grachev et al., 2013, 2007) were most likely affected by a large number of small-  
 723 scale, non-Kolomogorov turbulence data.  
 724



725  
 726 **Fig. 12.** The non-dimensional vertical gradient of wind speed plotted versus stability for two different  
 727 regimes: subcritical ( $Rf \leq 0.25$ , green) and supercritical ( $Rf > 0.25$ , violet). Error bars indicate one  
 728 standard deviation within each bin. Thick dashed line indicates the linear relationship (6) (Dyer, 1974); the  
 729 thin dashed line is the best fit to our data for  $Rf \leq 0.25$  (in the stability range  $0.005 < \zeta < 2.43$ ), while the  
 730 bold solid line corresponds to Eq. (7) (Beljaars and Holtslag, 1991).  
 731

732 Ha et al. (2007) evaluated surface layer similarity theory for different wind regimes in the nocturnal  
 733 boundary layer based on the CASES-99 data. They concluded that although the stability parameter is  
 734 inversely correlated to the mean wind speed, the speed of the large-scale flow has an independent role on the  
 735 flux-gradient relationship. For strong and intermediate wind classes, they found that  $\phi_m$  obeyed existing  
 736 stability functions when  $z/L$  is less than unity, while for weak mean wind and/or strong stability ( $z/L > 1$ )  
 737 similarity theory broke down. Following their approach, we evaluated the flux-gradient relationship  
 738 separately for different wind regimes, which were classified based on the mean wind speed at each level  
 739 similarly as in the study of Ha et al. (2007), and discriminated between subcritical and supercritical regimes.  
 740 The striking difference of the behavior of  $\phi_m$  with stability for different wind classes, which was found in

741 the study of Ha et al. (2007), cannot be observed in our dataset (Fig. 13). In the weak wind regime the scatter  
 742 is largest, although we have noted substantial scatter even for the intermediate and strong classes, caused by  
 743 the small scale turbulence, which survived even in the supercritical regime (violet symbols). If we consider  
 744 only data for  $Rf \leq 0.25$ , they follow Dyer's linear prediction even for the weak wind regime, indicating that  
 745 similarity theory holds in this regime for the whole range of stabilities.  
 746



747  
 748 **Fig. 13.** Non-dimensional vertical gradient of wind speed for each level plotted versus local stability  
 749 parameter for weak-, intermediate- and strong wind regimes, respectively. Individual data points for each  
 750 level are shown with the corresponding symbol. Data points exceeding critical value of  $Rf_{cr} = 0.25$   
 751 (supercritical regime) are shown in violet. Dashed line indicates the linear relationship of Dyer (1974) (Eq.  
 752 (6)) and the solid line corresponds to the relationship (7) (Beljaars and Holtslag, 1991).  
 753

754 We now turn to the self-correlation analysis. Since the present data exhibit different behavior for the  
 755 subcritical and supercritical regimes, the self-correlation analysis was performed separately for each of these  
 756 regimes. Linear correlation coefficients between  $\phi_m$  and  $\zeta$  for the original data and random data sets were  
 757 calculated for each level. Table 5 shows the impact of self-correlation on the dimensionless wind shear.  
 758 Generally, the results for both the sub- and supercritical regimes suggest a non-negligible but not decisive  
 759 impact of self-correlation. There are, however, two exceptions. At the lowest level, the subcritical data  
 760 mostly reflect the near-neutral range where large scatter of the data is present resulting in a relatively small  
 761 correlation coefficient of 0.54. Hence the self-correlation test, which is based on linear correlation, produces  
 762 small correlations of similar magnitudes for both physical and random data. This in turn results in a very  
 763 small value of  $R_{data}^2 - \langle R_{rand}^2 \rangle$  which means that results of this test are not very conclusive. At level 5, the

764 correlation coefficient is large in the subcritical regime and reduced in the supercritical due to the increased  
765 scatter of the data for  $\zeta > 1.5$  in this regime. Consequently, the value of  $R_{data}^2 - \langle R_{rand}^2 \rangle$  is small. For the  
766 three middle levels,  $R_{data}$  has similar values in both the subcritical and supercritical regime, since in both  
767 regimes they exhibit a strong positive fit, i.e.  $\phi_m$  increases with increasing stability with the larger scatter  
768 observed at level 4 (Fig. 12).

769

770 **Table 5**

771 Self-correlation analysis.  $R_{data}$  is a linear correlation coefficient between  $\phi_m$  and  $\zeta$  for the original data at  
772 each level.  $\langle R_{rand} \rangle$  is the self-correlation and it is the average of the correlation coefficients for 1000  
773 random datasets.  $R_{data}^2 - \langle R_{rand}^2 \rangle$  is a measure of the true physical variance explained by the linear model  
774 as proposed by Klipp and Mahrt (2004). Standard deviations are also indicated. N is the number of 30-min  
775 intervals.

Subcritical	N	$R_{data}$	$\langle R_{rand} \rangle$	$\sigma \langle R_{rand} \rangle$	$R_{data}^2 - \langle R_{rand}^2 \rangle$	$\sigma(R_{data}^2 - \langle R_{rand}^2 \rangle)$
Level 1	93	0.54	0.51	0.14	0.01	0.14
Level 2	83	0.91	0.55	0.11	0.50	0.12
Level 3	78	0.95	0.49	0.11	0.64	0.11
Level 4	60	0.73	0.49	0.13	0.28	0.13
Level 5	52	0.97	0.49	0.14	0.68	0.13
<b>Supercritical</b>						
Level 1	7	0.91	0.68	0.22	0.33	0.25
Level 2	17	0.91	0.51	0.18	0.54	0.18
Level 3	22	0.92	0.55	0.18	0.51	0.19
Level 4	39	0.66	0.43	0.15	0.22	0.13
Level 5	48	0.57	0.41	0.14	0.14	0.12

776

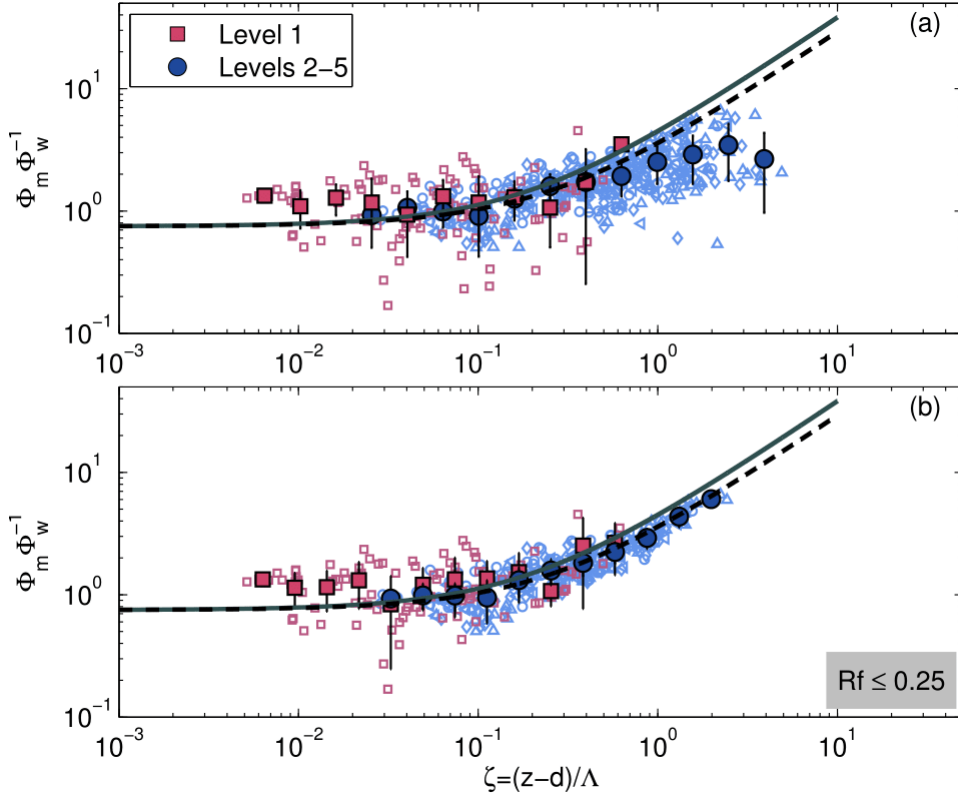
777

778 Grachev et al. (2013) proposed a new method which is not influenced by self-correlation and for which  
779  $z$ -less scaling should also be valid. This new function represents a combination of universal functions and is  
780 thus a universal function itself. This new function,

$$\phi_m \phi_w^{-1} = 0.75(1 + 5\zeta) \quad (18)$$

781 where the value of  $\phi_w = 1.33$  corresponds to the median value in the subcritical regime found in the study  
782 of Grachev et al. (2013) (Fig. 14, gray solid line). For our data, the median  $\phi_w$  value for levels 2–5 was also  
783 found to be equal to 1.33 in the subcritical regime. According to Fig. 14a, the increase of  $\phi_m \phi_w^{-1}$  with  
784 stability is slower than the linear prediction (solid and dashed lines, respectively). Due to the fact that this  
785 new similarity function  $\phi_m \phi_w^{-1}$  shares no variable with the stability parameter (except the reference height  
786  $z-d$ ), the observed decrease below the linear prediction is not caused by self-correlation. As seen from Fig.  
787 14b, this deviation from the linear relationship is mainly due to the small scale turbulence in the supercritical

788 regime ( $Rf > 0.25$ ). Additionally, this function is consistent with the  $z$ -less scaling when the prerequisite  
 789  $Rf \leq 0.25$  is imposed on the data (Fig. 14b). As already noted, the RSL shows a more pronounced influence  
 790 on the  $\phi_w$  profile compared to the wind shear profile, thus leading to an overestimation of Eq. (18) at level 1  
 791 while no systematic deviation can be observed for levels 2–5 (Fig. 14). The scatter in the near-neutral range  
 792 at level 1 could be partly due to the wind direction inhomogeneities (not shown).  
 793



794  
 795 **Fig. 14.** The bin-averaged non-dimensional function  $\phi_m \phi_w^{-1} = \frac{k(z-d)}{\sigma_w} \frac{dU}{dz}$ , which is not influenced by self-  
 796 correlation, plotted versus local stability. Individual data for each level are shown in the corresponding  
 797 symbol as in Fig. 4. Bin averages for the lowest level (red squares) and four higher levels (blue circles) are  
 798 included for easier interpretation of trends. Error bars indicate one standard deviation within each bin. Gray  
 799 line corresponds to the experimental fit according to Grachev et al. (2013) ( $\phi_m \phi_w^{-1} = 0.75(1 + 5\zeta)$ ) and the  
 800 dashed black line is the best fit to our data ( $\phi_m \phi_w^{-1} = 0.75(1 + 3.8\zeta)$ ) in the subcritical regime. (b) Same  
 801 as (a) but subject to the condition  $Rf \leq 0.25$ .  
 802

## 803 5. Summary and Conclusions

804 Multi-level measurements of atmospheric turbulence carried out over a heterogeneous surface in the  
 805 continental part of Croatia have been used to study turbulence characteristics in the wintertime nocturnal  
 806 boundary layer. Measurements that were obtained from five levels in the layer between 20 and 62 m above

807 the ground and 2–44 m above the local canopy height, provided valuable insight in the turbulence  
808 characteristics within tens of meters above the ground level. We focused on evaluating the applicability of  
809 local similarity scaling approach, in terms of flux-variance and flux-gradient similarity, over spatially  
810 inhomogeneous surface characteristics.

811 Due to specific local terrain characteristics and distinctive features of the stable boundary layer (SBL),  
812 special attention was given to data quality control and post-processing options, which included  
813 determination of appropriate turbulence averaging time scale for defining turbulence fluctuations, testing the  
814 stationarity of the data and invoking an uncertainty test. Observations were conducted inside (the lowest  
815 observational level) and above the roughness sublayer (RSL).

816 After removing highly uncertain data points (uncertainty threshold > 50 %), when assessing scaling  
817 under inhomogeneous fetch conditions in the SBL, dimensionless standard deviations of wind velocity  
818 components were found to behave differently than the dimensionless wind shear. Concerning the normalized  
819 standard deviations, it was found that vertical velocity shows a tendency to “ideal” behavior, that is, it  
820 follows  $z$ -less scaling when approaching large stability. The longitudinal and transversal components show a  
821 dependency on stability, with the latter exhibiting a more pronounced linear increase with increasing  
822 stability. Consequently, scaled turbulent kinetic energy was found to have a linear dependence on the  
823 stability parameter in the range  $0.05 \leq \zeta \leq 10$  for levels above the RSL. However, we found local scaling  
824 to be valid for all three variables, which is astonishing given the complex and spatially inhomogeneous  
825 surface characteristics. For neutral conditions, due to the RSL influence values of all three non-dimensional  
826 velocity variances were found to be smaller at the lowest measurement level, while these were larger at  
827 higher levels in comparison with values obtained for HHF terrain.

828 The ratio of the observed dimensionless standard deviation of the vertical wind component and  
829 corresponding values of commonly used similarity formulas over horizontally homogeneous and flat (HHF)  
830 terrain showed considerable variation with wind direction, indicating the influence of surface roughness  
831 changes and topography. Therefore, we separately analyzed velocity variances for different wind directions  
832 corresponding to undistorted ( $\phi_w/\phi_{w(HHF)} \approx 1$ ) and distorted ( $\phi_w/\phi_{w(HHF)} \neq 1$ ) sectors, respectively.  
833 Differences between these sectors at the lowest level were only found in the near-neutral regime with larger  
834 magnitudes for the distorted sectors. At upper levels, dimensionless longitudinal and vertical wind variances  
835 also showed higher values for these wind directions. However, this did not influence results regarding the

836 relationship with stability. For non-dimensional velocity variances, and consequently non-dimensional TKE  
837 and the momentum and heat flux correlation coefficients, no discernible difference between sub- and  
838 supercritical regimes was observed.

839 Results for the non-dimensional wind shear appear to be less sensitive to inhomogeneous site  
840 characteristics. Despite the largely inhomogeneous surface characteristics at the measuring site, flux-gradient  
841 relationship showed a similar distinction between Kolmogorov and non-Kolmogorov turbulence as found  
842 under ideal (HHF) conditions (Grachev et al., 2013). Our results support the classical Businger-Dyer linear  
843 expression for the non-dimensional profile of wind speed, with slightly different best-fit coefficient, even  
844 over inhomogeneous terrain but only after removing data which correspond to the flux Richardson number  
845  $Rf > 0.25$ . Hence, our data follow local  $z$ -less scaling for the  $\phi_m$  function when the condition  $Rf = 0.25$  is  
846 imposed. Similar to HHF conditions, supercritical ( $Rf > 0.25$ ) data show a leveling-off for  $\phi_m$  at higher  
847 stability thus seemingly supporting the non-linear relationship of Beljaars and Holtslag (1991). Therefore,  
848 we conclude that the non-dimensional wind shear over a largely heterogeneous vegetated surface is only  
849 weakly, if at all, affected by the surface inhomogeneity. Thus, when interested in only subcritical, fully  
850 turbulent conditions, the classical linear formulation for  $\phi_m$  is appropriate. Correspondingly, if all  
851 turbulence states (regardless of sub- or supercritical) are of interest, the Beljaars-Holtslag formulation is to  
852 be preferred. Finally, we investigate whether the wind magnitude has an impact on the distinction between  
853 Kolmogorov and non-Kolmogorov turbulence. The flux-gradient dependence on stability did not show  
854 different behavior for different wind regimes, indicating that the stability parameter is sufficient predictor for  
855 flux-gradient relationship.

856 Overall, the present stable night-time results from a forested site with highly inhomogeneous fetch  
857 conditions show that flux-variance relationships obey local scaling but the corresponding non-dimensional  
858 functions do not exhibit the same parameter values as over HHF terrain. The  $z$ -less limes for strong stability  
859 is assumed by the vertical and to somewhat lesser degree by the horizontal velocity fluctuations. The RSL  
860 influence appears to be larger than the distortion due to inhomogeneous surface conditions. Flux-gradient  
861 relationships, on the other hand, seem to be less influenced by surface inhomogeneity: they exhibit the same  
862 distinction into sub- and supercritical turbulence regimes as over HHF terrain. For both, subcritical  
863 turbulence alone and “all conditions” the data follow quite closely the respective functions from the  
864 literature. Finally, no distinct impact of the RSL can be observed for the flux-gradient relations.

866 **Acknowledgements:** We would like to acknowledge Željko Večenaj's crucial role in the setting up  
 867 instruments and maintenance of the measurement site. We are also thankful for his assistance in the  
 868 application of MFD and stationarity analysis. We are grateful to Branko Grisogono for providing two sonic  
 869 anemometers for the use in this experiment. We gratefully acknowledge two anonymous reviewers whose  
 870 comments led to the improvement of the manuscript. The study was supported by the Croatian Ministry of  
 871 Science, Education and Sports (grant No. 119-1193086-1323). The first author's research visit at Institute of  
 872 Atmospheric and Cryospheric Sciences, University of Innsbruck was supported by the Austrian Federal  
 873 Ministry of Science, Research and Economy (BMWFW) through Ernst Mach Grant – Worldwide program.

## 875 **References**

- 876 Andreas, E.L., Hill, R.J., Gosz, J.R., Moore, D.I., Otto, W.D., Sarma, A.D., 1998a. Statistics of  
 877 surface-layer turbulence over terrain with metre-scale heterogeneity. *Boundary-Layer*  
 878 *Meteorol.* 86, 379–408. doi:10.1023/A:1000609131683
- 879 Aubinet, M., Vesala, T., Papale, D., 2012. *Eddy Covariance: A Practical Guide to Measurement*  
 880 *and Data Analysis*. Springer.
- 881 Baas, P., Steeneveld, G.J., van de Wiel, B.J.H., Holtslag, A.A.M., 2006. Exploring self-correlation  
 882 in flux-gradient relationships for stably stratified conditions. *J. Atmos. Sci.* 63, 3045–3054.  
 883 doi:10.1175/JAS3778.1
- 884 Babić, K., Klaić, Z.B., Večenaj, Ž., 2012. Determining a turbulence averaging time scale by Fourier  
 885 analysis for the nocturnal boundary layer. *Geofizika* 29, 35–51.
- 886 Babić, N., Večenaj, Ž., De Wekker, S.F.J., 2016. Flux–variance similarity in complex terrain and  
 887 its sensitivity to different methods of treating non-stationarity. *Boundary-Layer Meteorol.* 159,  
 888 123–145. doi:10.1007/s10546-015-0110-0
- 889 Basu, S., Porté-Agel, F., Fofoula-Georgiou, E., Vinuesa, J.F., Pahlow, M., 2006. Revisiting the  
 890 local scaling hypothesis in stably stratified atmospheric boundary-layer turbulence: An  
 891 integration of field and laboratory measurements with large-eddy simulations. *Boundary-*  
 892 *Layer Meteorol.* 119, 473–500. doi:10.1007/s10546-005-9036-2
- 893 Beljaars, A.C.M., Holtslag, A.A.M., 1991. Flux parameterization over land surfaces for  
 894 atmospheric models. *J. Appl. Meteorol.* doi:10.1175/1520-  
 895 0450(1991)030<0327:FPOLSF>2.0.CO;2
- 896 Bosveld, F.C., 1997. Derivation of fluxes from profiles over a moderately homogeneous forest.  
 897 *Boundary-Layer Meteorol.* 84, 289–327. doi:10.1023/A:1000453629876
- 898 Bou-Zeid, E., Parlange, M.B., Meneveau, C., 2007. On the parameterization of surface roughness at  
 899 regional scales. *J. Atmos. Sci.* 64, 216–227. doi:10.1175/JAS3826.1
- 900 Businger, J.A., Wyngaard, J.C., Izumi, Y., Bradley, E.F., 1971. Flux-profile relationships in the  
 901 atmospheric surface layer. *J. Atmos. Sci.* doi:10.1175/1520-  
 902 0469(1971)028<0181:FPRITA>2.0.CO;2
- 903 Calaf, M., Higgins, C., Parlange, M.B., 2014. Large wind farms and the scalar flux over an  
 904 heterogeneously rough land surface. *Boundary-Layer Meteorol.* 153, 471–495.  
 905 doi:10.1007/s10546-014-9959-6
- 906 Cheng, H., Castro, I.P., 2002. Near-wall flow development after a step change in surface roughness.  
 907 *Boundary-Layer Meteorol.* 105, 411–432. doi:10.1023/A:1020355306788

- 908 Cheng, Y., Brutsaert, W., 2005. Flux-profile relationships for wind speed and temperature in the  
909 stable atmospheric boundary layer. *Boundary-Layer Meteorol.* 114, 519–538.
- 910 Cheng, Y., Parlange, M.B., Brutsaert, W., 2005. Pathology of Monin-Obukhov similarity in the  
911 stable boundary layer. *J. Geophys. Res. Atmos.* 110, D06101. doi:10.1029/2004JD004923
- 912 Conangla, L., Cuxart, J., Soler, M.R., 2008. Characterisation of the nocturnal boundary layer at a  
913 site in Northern Spain. *Boundary-Layer Meteorol.* 128, 255–276. doi:10.1007/s10546-008-  
914 9280-3
- 915 de Franceschi, M., Zardi, D., Tagliazucca, M., Tampieri, F., 2009. Analysis of second-order  
916 moments in surface layer turbulence in an Alpine valley. *Q. J. R. Meteorol. Soc.* 135, 1750–  
917 1765. doi:10.1002/qj.506
- 918 Dellwik, E., Jensen, N.O., 2005. Flux–Profile relationships over a fetch limited beech forest.  
919 *Boundary-Layer Meteorol.* 115, 179–204. doi:10.1007/s10546-004-3808-y
- 920 Derbyshire, S.H., 1995. Stable boundary layers: Observations, models and variability part I:  
921 Modelling and measurements. *Boundary-Layer Meteorol.* 74, 19–54.
- 922 Dyer, A.J., 1974. A review of flux-profile relationships. *Boundary-Layer Meteorol.* 7, 363–372.  
923 doi:10.1007/BF00240838
- 924 Finnigan, J., 2000. Turbulence in plant canopies. *Annu. Rev. Fluid Mech.* 32, 519–571.  
925 doi:10.2480/agrmet.20.1
- 926 Finnigan, J.J., Shaw, R.H., 2000. A wind-tunnel study of airflow in waving wheat: an EOF analysis  
927 of the structure of the large-eddy motion. *Boundary-layer Meteorol.* 96, 211–255.  
928 doi:10.1023/A:1002618621171
- 929 Foken, T., 2008. *Micrometeorology*. Springer-Verlag Berlin Heidelberg.
- 930 Foken, T., Wichura, B., 1996. Tools for quality assessment of surface-based flux measurements.  
931 *Agric. For. Meteorol.* 78, 83–105.
- 932 Forrer, J., Rotach, M.W., 1997. On the turbulence structure in the stable boundary layer over the  
933 greenland ice sheet. *Boudary-Layer Meteorology* 85, 111–136.
- 934 Fortuniak, K., Pawlak, W., Siedlecki, M., 2013. Integral turbulence statistics over a Central  
935 European city Centre. *Boundary-Layer Meteorol.* 146, 257–276. doi:10.1007/s10546-012-  
936 9762-1
- 937 Grachev, A.A., Andreas, E.L., Fairall, C.W., Guest, P.S., Persson, P.O.G., 2015. Similarity theory  
938 based on the Dougherty-Ozmidov length scale. *Q. J. R. Meteorol. Soc.* 141, 1845–1856.  
939 doi:10.1002/qj.2488
- 940 Grachev, A.A., Andreas, E.L., Fairall, C.W., Guest, P.S., Persson, P.O.G., 2013. The critical  
941 Richardson number and limits of applicability of local similarity theory in the stable boundary  
942 layer. *Boundary-Layer Meteorol.* 147, 51–82. doi:10.1007/s10546-012-9771-0
- 943 Grachev, A.A., Andreas, E.L., Fairall, C.W., Guest, P.S., Persson, P.O.G., 2007. SHEBA flux-  
944 profile relationships in the stable atmospheric boundary layer. *Boundary-Layer Meteorol.* 124,  
945 315–333. doi:10.1007/s10546-007-9177-6
- 946 Ha, K.-J., Hyun, Y.-K., Oh, H.-M., Kim, K.-E., Mahrt, L., 2007. Evaluation of boundary layer  
947 similarity theory for stable conditions in CASES-99. *Mon. Weather Rev.* 135, 3474–3483.  
948 doi:10.1175/MWR3488.1
- 949 Harman, I.N., Finnigan, J.J., 2010. Flow over hills covered by a plant canopy: Extension to  
950 generalised two-dimensional topography. *Boundary-Layer Meteorol.* 135, 51–65.  
951 doi:10.1007/s10546-009-9458-3
- 952 Hicks, B., 1978. Some limitations of dimensional analysis and power laws. *Boundary-Layer*  
953 *Meteorol* 14, 567–569. doi:10.1007/BF00121895
- 954 Högström, U., 1988. Non-dimensional wind and temperature profiles in the atmospheric surface  
955 layer: A re-evaluation. *Boundary-Layer Meteorol.* 42, 55–78. doi:10.1007/BF00119875
- 956 Högström, U., Bergström, H., Smedman, A.S., Halldin, S., Lindroth, A., 1989. Turbulent exchange  
957 above a pine forest, I: Fluxes and gradients. *Boundary-Layer Meteorol.* 49, 197–217.  
958 doi:10.1007/BF00116411
- 959 Holtslag, A.A.M., Nieuwstadt, F.T.M., 1986. Scaling the atmospheric boundary layer. *Boundary-*



960 Layer Meteorol. 36, 201–209. doi:10.1007/BF00117468

961 Howell, J., Mahrt, L., 1997. Multiresolution flux decomposition. *Boundary-Layer Meteorol.* 83,

962 117–137. doi:10.1023/A:1000210427798

963 Howell, J.F., Sun, J., 1999. Surface-layer fluxes in stable conditions. *Boundary-Layer Meteorol.* 90,

964 495–520. doi:10.1023/A:1001788515355

965 Kaimal, J.C., 1973. Turbulence spectra, length scales and structure parameters in the stable surface

966 layer. *Boundary-Layer Meteorol.* 4, 289–309. doi:10.1007/BF02265239

967 Kaimal, J.C., Finnigan, J.J., 1994. *Atmospheric boundary layer flows: Their structure and*

968 *measurement.* University Press, New York.

969 Kaimal, J.C., Wyngaard, J.C., 1990. The Kansas and Minnesota Experiments. *Boundary-Layer*

970 *Meteorology* 50, 31–47.

971 Katul, G., Goltz, S.M., Hsieh, C.-I., Cheng, Y., Mowry, F., Sigmon, J., 1995. Estimation of surface

972 heat and momentum fluxes using the flux-variance method above uniform and non-uniform

973 terrain. *Boundary-Layer Meteorol.* 74, 237–260. doi:10.1007/BF00712120

974 Katul, G., Hsieh, C.I., Bowling, D., Clark, K., Shurpali, N., Turnipseed, A., Albertson, J., Tu, K.,

975 Hollinger, D., Evans, B., Offerle, B., Anderson, D., Ellsworth, D., Vogel, C., Oren, R., 1999.

976 Spatial variability of turbulent fluxes in the roughness sublayer of an even-aged pine forest.

977 *Boundary-Layer Meteorol.* 93, 1–28. doi:10.1023/A:1002079602069

978 Klipp, C.L., Mahrt, L., 2004. Flux-gradient relationship, self-correlation and intermittency in the

979 stable boundary layer. *Q. J. R. Meteorol. Soc.* 130, 2087–2103. doi:10.1256/qj.03.161

980 Kljun, N., Calanca, P., Rotach, M.W., Schmid, H.P., 2015. A simple two-dimensional

981 parameterisation for Flux Footprint Prediction (FFP). *Geosci. Model Dev.* 8, 3695–3713.

982 doi:10.5194/gmd-8-3695-2015

983 Kral, S.T., Sjöblom, A., Nygård, T., 2014. Observations of summer turbulent surface fluxes in a

984 High Arctic fjord. *Q. J. R. Meteorol. Soc.* 140, 666–675. doi:10.1002/qj.2167

985 Mahrt, L., 2014. Stably stratified atmospheric boundary layers. *Annu. Rev. Fluid Mech.* 46, 23–45.

986 doi:10.1146/annurev-fluid-010313-141354

987 Mahrt, L., 2011. The near-calm stable boundary layer. *Boundary-Layer Meteorol.* 140, 343–360.

988 doi:10.1007/s10546-011-9616-2

989 Mahrt, L., 2007. The influence of nonstationarity on the turbulent flux-gradient relationship for

990 stable stratification. *Boundary-Layer Meteorol.* 125, 245–264. doi:10.1007/s10546-007-9154-0

991 Mahrt, L., 2000. Surface heterogeneity and vertical structure of the boundary layer. *Boundary-*

992 *Layer Meteorol.* 96, 33–62. doi:10.1023/A:1002482332477

993 Mahrt, L., Thomas, C., Richardson, S., Seaman, N., Stauffer, D., Zeeman, M., 2013. Non-stationary

994 generation of weak turbulence for very stable and weak-wind conditions. *Boundary-Layer*

995 *Meteorol.* 147, 179–199. doi:10.1007/s10546-012-9782-x

996 Mahrt, L., Vickers, D., Frederickson, P., Davidson, K., Smedman, A.-S., 2003. Sea-surface

997 aerodynamic roughness. *J. Geophys. Res.* 108(C6), 3171. doi:10.1029/2002JC001383

998 Malhi, Y., 1996. The behaviour of the roughness length for temperature over heterogeneous

999 surfaces. *Q. J. R. Meteorol. Soc.* 122, 1095–1125.

1000 Marques Filho, E.P., Sá, L.D.A., Karam, H.A., Alvalá, R.C.S., Souza, A., Pereira, M.M.R., 2008.

1001 Atmospheric surface layer characteristics of turbulence above the Pantanal wetland regarding

1002 the similarity theory. *Agric. For. Meteorol.* 148, 883–892.

1003 doi:10.1016/j.agrformet.2007.12.004

1004 Martins, C.A., Moraes, O.L.L., Acevedo, O.C., Degrazia, G.A., 2009. Turbulence intensity

1005 parameters over a very complex terrain. *Boundary-Layer Meteorol.* 133, 35–45.

1006 doi:10.1007/s10546-009-9413-3

1007 Miller, N.E., Stoll, R., 2013. Surface heterogeneity effects on regional-scale fluxes in the stable

1008 boundary layer: Aerodynamic roughness length transitions. *Boundary-Layer Meteorol.* 149,

1009 277–301. doi:10.1007/s10546-013-9839-5

1010 Mironov, D. V., Sullivan, P.P., 2010. Effect of horizontal surface temperature heterogeneity on

1011 turbulent mixing in the stably stratified atmospheric boundary layer. *19th Amer. Meteorol.*

- 1012 Soc. Symp. Bound. Layers Turbul. CO, USA, 10 pp.
- 1013 Mölder, M., Grelle, A., Lindroth, A., Halldin, S., 1999. Flux-profile relationships over a boreal  
1014 forest - Roughness sublayer corrections. *Agric. For. Meteorol.* 98-99, 645–658.  
1015 doi:10.1016/S0168-1923(99)00131-8
- 1016 Monin, A.S., Obukhov, A.M., 1954. Basic laws of turbulent mixing in the surface layer of the  
1017 atmosphere. *Contrib. Geophys. Inst. Acad. Sci. USSR* 24, 163–187.
- 1018 Monteith, J.L., Unsworth, M.H., 1990. *Principles of Environmental Physics*, 2nd ed. Edward  
1019 Arnold, London.
- 1020 Moraes, O.L.L., Acevedo, O.C., Degrazia, G.A., Anfossi, D., da Silva, R., Anabor, V., 2005.  
1021 Surface layer turbulence parameters over a complex terrain. *Atmos. Environ.* 39, 3103–3112.  
1022 doi:10.1016/j.atmosenv.2005.01.046
- 1023 Nadeau, D.F., Pardyjak, E.R., Higgins, C.W., Parlange, M.B., 2013. Similarity scaling over a steep  
1024 alpine slope. *Boundary-Layer Meteorol.* 147, 401–419. doi:10.1007/s10546-012-9787-5
- 1025 Nakamura, R., Mahrt, L., 2001. Similarity theory for local and spatially averaged momentum  
1026 fluxes. *Agric. For. Meteorol.* 108, 265–279.
- 1027 Nieuwstadt, F.T.M., 1984. The turbulent structure of the stable, nocturnal boundary layer. *J. Atmos.*  
1028 *Sci.* doi:10.1175/1520-0469(1984)041<2202:TTSOTS>2.0.CO;2
- 1029 Obukhov, A.M., 1946. Turbulence in an atmosphere with a non-uniform temperature. *Boundary-*  
1030 *Layer Meteorol.* 2, 7–29.
- 1031 Pahlow, M., Parlange, M.B., Porté-Agel, F., 2001. On Monin–Obukhov similarity in the stable  
1032 atmospheric boundary layer. *Boundary-Layer Meteorol.* 99, 225–248.
- 1033 Panofsky, H.A., Dutton, J.A., 1984. *Atmospheric Turbulence: Models and Methods for*  
1034 *Engineering Applications*. John Wiley and Sons, New York.
- 1035 Rannik, Ü., 1998. On the surface layer similarity at a complex forest site. *J. Geophys. Res.* 103,  
1036 8685–8697.
- 1037 Raupach, M.R., 1994. Simplified expressions for vegetation roughness length and zero-plane  
1038 displacement as function of canopy height and area index. *Boundary-Layer Meteorol.* 71, 211–  
1039 216.
- 1040 Raupach, M.R., 1979. Anomalies in flux-gradient relationships over forest. *Boundary-Layer*  
1041 *Meteorol.* 16, 467–486.
- 1042 Raupach, M.R., Finnigan, J.J., Brunet, Y., 1996. Coherent eddies and turbulence in vegetation  
1043 canopies: The mixing-layer analogy. *Boundary-Layer Meteorol.* 78, 351–382.
- 1044 Rotach, M.W., 1993. Turbulence close to a rough urban surface. Part II: Variances and gradients.  
1045 *Boundary-Layer Meteorol.* 66, 75–92.
- 1046 Rotach, M.W., Andretta, M., Calanca, P., Weigel, A.P., Weiss, A., 2008. Boundary layer  
1047 characteristics and turbulent exchange mechanisms in highly complex terrain. *Acta Geophys.*  
1048 56, 194–219. doi:10.2478/s11600-007-0043-1
- 1049 Rotach, M.W., Calanca, P., 2014. *Microclimate*. Academic Press, pp. 258–264.
- 1050 Rotach, M.W., Calanca, P., Graziani, P., Gurtz, J., Steyn, D.G., Vogt, R., Andretta, M., Christen,  
1051 A., Cieslik, S., Connolly, R., De Wekker, S.F.J. and Galmarini, S., Kadygrov, E.N.,  
1052 Kadygrov, V., Miller, E., Neininger, B., Rucker, M., van Gorsel, E., Weber, H., Weiss, A.,  
1053 Zappa, M., 2004. Turbulence structure and exchange processes in an Alpine Valley: The  
1054 Riviera project. *Bull. Am. Meteorol. Soc.* 85, 1367–1385. doi:10.1175/BAMS-85-9-1367
- 1055 Sanz Rodrigo, J., Anderson, P.S., 2013. Investigation of the stable atmospheric boundary layer at  
1056 Halley Antarctica. *Boundary-Layer Meteorology* 148, 517–539. doi:10.1007/s10546-013-9831-0
- 1057 Shaw, R.H., Finnigan, J.J., Patton, E.G., 2006. Eddy structure near the plant canopy interface. 17th  
1058 Symp. Bound. Layers Turbul. J2.1.
- 1059 Simpson, I.J., Thurtell, G.W., Neumann, H.H., Den Hartog, G., Edwards, G.C., 1998. The validity  
1060 of similarity theory in the roughness sublayer above forests. *Boundary-Layer Meteorol.* 87,  
1061 69–99. doi:10.1023/A:1000809902980
- 1062 Sorbjan, Z., Grachev, A.A., 2010. An evaluation of the flux – gradient relationship in the stable  
1063 boundary layer. *Boundary-Layer Meteorol.* 135, 385–405. doi:10.1007/s10546-010-9482-3

1064 Stiperski, I., Rotach, M.W., 2016. On the measurement of turbulence over complex mountainous  
1065 terrain. *Boundary-Layer Meteorol.* 159, 97–121. doi:10.1007/s10546-015-0115-8  
1066 Stoll, R., Porté-Agel, F., 2008. Large-eddy simulation of the stable atmospheric boundary layer  
1067 using dynamic models with different averaging schemes. *Boundary-Layer Meteorol.* 126, 1–  
1068 28. doi:10.1007/s10546-007-9207-4  
1069 Stull, R.B., 1988. *An Introduction to Boundary-Layer Meteorology*. Kluwer Academic Publishers,  
1070 Dordrecht.  
1071 Thom, A.S., Stewart, J.B., Oliver, H.R., Gash, J.H.C., 1975. Comparison of aerodynamic and  
1072 energy budget estimates of fluxes over a pine forest. *Q. J. R. Meteorol. Soc.* 101, 93–105.  
1073 doi:10.1002/qj.49710142708  
1074 Trini Castelli, S., Falabino, S., 2013. Analysis of the parameterization for the wind-velocity  
1075 fluctuation standard deviations in the surface layer in low-wind conditions. *Meteorol. Atmos.*  
1076 *Phys.* 119, 91–107. doi:10.1007/s00703-012-0219-3  
1077 Večenaj, Ž., De Wekker, S.F.J., 2015. Determination of non-stationarity in the surface layer during  
1078 the T-REX experiment. *Q. J. R. Meteorol. Soc.* 141, 1560–1571. doi:10.1002/qj.2458  
1079 Vickers, D., Mahrt, L., 2003. The cospectral gap and turbulent flux calculations. *J. Atmos. Ocean.*  
1080 *Technol.* 20, 660–672. doi:10.1175/1520-0426(2003)20<660:TCGATF>2.0.CO;2  
1081 Wilczak, J., Oncley, S., Stage, S., 2001. Sonic anemometer tilt correction algorithms. *Boundary-*  
1082 *Layer Meteorol.* 99, 127–150. doi:10.1023/A:1018966204465  
1083 Wood, C.R., Lacser, A., Barlow, J.F., Padhra, A., Belcher, S.E., Nemitz, E., Helfter, C., Famulari,  
1084 D., Grimmond, C.S.B., 2010. Turbulent flow at 190 m height above London during 2006-  
1085 2008: A climatology and the applicability of similarity theory. *Boundary-Layer Meteorol.* 137,  
1086 77–96. doi:10.1007/s10546-010-9516-x  
1087 Wyngaard, J.C., Coté, O.R., 1972. Cospectral similarity in the atmospheric surface layer. *Q. J. R.*  
1088 *Meteorol. Soc.* 98, 590–603. doi:10.1002/qj.49709841708  
1089  
1090